NASA/TP-2019-220401

Effects of the Serber First Step in 3DHZETRN-v2.1

John W. Wilson
Old Dominion University, Norfolk, Virginia

Charles M. Werneth and Tony C. Slaba
Langley Research Center, Hampton, Virginia

Francis F. Badavi
Old Dominion University, Norfolk, Virginia

Brandon D. Reddell
Johnson Space Center, Houston, Texas

Amir A. Bahadori
Kansas State University, Manhattan, Kansas

September 2019

NASA STI Program . . . in Profile

Since its founding, NASA has been dedicated to the advancement of aeronautics and space science. The NASA scientific and technical information (STI) program plays a key part in helping NASA maintain this important role.

The NASA STI program operates under the auspices of the Agency Chief Information Officer. It collects, organizes, provides for archiving, and disseminates NASA's STI. The NASA STI program provides access to the NTRS Registered and its public interface, the NASA Technical Reports Server, thus providing one of the largest collections of aeronautical and space science STI in the world. Results are published in both non-NASA channels and by NASA in the NASA STI Report Series, which includes the following report types:

- TECHNICAL PUBLICATION. Reports of completed research or a major significant phase of research that present the results of NASA Programs and include extensive data or theoretical analysis. Includes compilations of significant scientific and technical data and information deemed to be of continuing reference value. NASA counter-part of peer-reviewed formal professional papers but has less stringent limitations on manuscript length and extent of graphic presentations.

- TECHNICAL MEMORANDUM. Scientific and technical findings that are preliminary or of specialized interest, e.g., quick release reports, working papers, and bibliographies that contain minimal annotation. Does not contain extensive analysis.

- CONTRACTOR REPORT. Scientific and technical findings by NASA-sponsored contractors and grantees.

- CONFERENCE PUBLICATION. Collected papers from scientific and technical conferences, symposia, seminars, or other meetings sponsored or co-sponsored by NASA.

- SPECIAL PUBLICATION. Scientific, technical, or historical information from NASA programs, projects, and missions, often concerned with subjects having substantial public interest.

- TECHNICAL TRANSLATION. English-language translations of foreign scientific and technical material pertinent to NASA's mission.

Specialized services also include organizing and publishing research results, distributing specialized research announcements and feeds, providing information desk and personal search support, and enabling data exchange services.

For more information about the NASA STI program, see the following:

- Access the NASA STI program home page at http://www.sti.nasa.gov

- E-mail your question to help@sti.nasa.gov

- Phone the NASA STI Information Desk at 757-864-9658

- Write to:
  NASA STI Information Desk
  Mail Stop 148
  NASA Langley Research Center
  Hampton, VA 23681-2199

NASA/TP–2019-220401

Effects of the Serber First Step in 3DHZETRN-v2.1

John W. Wilson
Old Dominion University, Norfolk, Virginia

Charles M. Werneth and Tony C. Slaba
Langley Research Center, Hampton, Virginia

Francis F. Badavi
Old Dominion University, Norfolk, Virginia

Brandon D. Reddell
Johnson Space Center, Houston, Texas

Amir A. Bahadori
Kansas State University, Manhattan, Kansas

National Aeronautics and
Space Administration

Langley Research Center
Hampton, Virginia 23681-2199

September 2019

Acknowledgments

This work was supported by the Human Research Program under the Human Exploration and Oper-ations Mission Directorate of NASA and by NASA Grant number NNX14AL77A.

Available from:

NASA STI Program / Mail Stop 148
NASA Langley Research Center
Hampton, VA 23681-2199
Fax: 757-864-6500

Contents

List of Figures

List of Tables

Abstract

3DHZETRN-v2 includes a detailed three dimensional (3D) treatment of neutron/light-ion transport based on a quasi-elastic/multiple-production assumption allowing improved agreement of the neutron/light-ion fluence compared with results of three Monte Carlo (MC) codes in the sense that the variance with respect to the individual MC results is less than the variance among the MC code results. The current numerical methods are no longer the main limitation to HZETRN code development and further changes in the nuclear model are required. In a prior study, an improved quasi-elastic spectrum based on a solution of the transport approximation to nuclear media effects showed promise, but the remaining multiple-production spectrum was based on a database derived from the Ranft model that used Bertini multiplicities. In the present paper, we will implement a more complete Serber first step into the 3DHZETRN-v2 code, but we retain the Bertini-Ranft branching ratios and evaporation multiplicities. It is shown that the new Serber model in the 3HZETRN-v2 code reduces the variance with individual MC codes, which are largely due to nuclear cross section model differences.

1. Introduction

Space radiation transport codes, such as the deterministic HZETRN code developed by NASA, require accurate nuclear cross section databases as input. But these databases did not exist during the first decade in which HZETRN was being developed. Even the perturbative approach developed for transport solutions to the Boltzmann equation within the straight-ahead approximation was based on simple nuclear data sets for 1 GeV protons interacting with tissue (Wilson and Lamkin, 1974). In that study, a straight-ahead Monte Carlo (MC) result utilizing the same data set (Wright et al., 1969) provided motivation for the development of more useful methods based on numerical procedures. A more complete study based on coupling of the neutron and proton field solutions (Lamkin, 1974; Wilson and Lamkin, 1975) resulted in a more computationally efficient solution to nucleon transport in extended materials than the more relatively inefficient MC methods. In addition to the use of numerical perturbation theory in nuclear transport algorithms, an even more efficient numerical marching procedure was derived for the transport of heavy-ions (Wilson, 1977).

In the mid-1970s, nuclear multiple scattering theory emerged as a theoretical basis for generating a database for heavy-ion interactions (Wilson, 1975; Wilson and Costner, 1975). An analytic solution of the heavy-ion perturbation transport theory was derived by employing a Rudstam related formalism (Silberberg et al., 1976) which was used to analyze high-energy/heavy-ion (HZE) experiments in extended targets (Wilson et al., 1984). Despite these developments, a more complete interaction database for nucleons and light-ions was needed to complete the description of HZE transport, apart from the effects of mesons. Moreover, a nucleonic transport marching algorithm that was more compatible with the HZE marching code was highly desirable, but such developments needed a more complete nucleon interaction database.

The work of Ranft (1980) that was used in early versions of FLUKA was an important functional set for developing nucleon transport marching procedures. In search of an improved nucleon interaction database, the Ranft spectral distributions were used with the direct (cascade) and evaporation multiplicities taken from Bertini (Anon., 1968; Bertini et al., 1969, 1972). A study of the transport procedure convergence that used a realistic interaction cross section (Wilson et al., 1988a) provided some confidence in the marching procedure (accuracy to < 1 percent difference for space boundary conditions compared with an analytic solution using realistic interaction). This verified marching procedure was then employed with the newly derived modified Ranft cross sections (Wilson et al., 1987a). However, these cross sections were not found to be in good agreement with MC results from the newly developed High Energy Transport Code (HETC) (Alsmiller, 1967). It was surmised that the Ranft formalism did give an adequate representation of the

evaporated and the constituent recoil nucleons but lacked an adequate representation of the quasi-elastic scattered nucleons. Hence, a crude approximation of the quasi-elastic contribution was added, which yielded improved agreement with the MC evaluations (Wilson et al., 1987a). This early work is recounted in Wilson et al. (1987a, 1988a,b, 1991), where this preliminary database was used for numerical algorithm studies. It further proved to be adequate for application to space systems design, where uncertainty was mainly associated with solution procedures that used the straight–ahead approximation rather than the nuclear database.

A progression of practical solutions for nucleon transport–from the simple straight-ahead approximation to increasingly complex formalisms–allowed for early implementation of high-performance computational procedures based on marching algorithms (Wilson et al., 1974, 1977, 1986, 1988a,b, 1991, 1994, 2006). The next step in transport code development was to represent the backward propagating components in a lowest order approximation (Clowdsley et al., 2000, 2001). This was accomplished by isolating the isotropic component of the modified Ranft cross sections into forward and backward propagating components. It was found that this code generally produced results for dosimetric quantities that agreed with MC codes to the extent that the MC codes agreed among themselves (Heinbockel et al., 2003, 2009; Slaba et al., 2010). This treatment represents the first step in a full three-dimensional (3D) code.

Subsequent development toward a 3D solution was accomplished by solving the isotropic distribution along a number of N-rays using the forward/backward propagator along each ray (Wilson et al., 2014a-c). This forward/isotropic solution showed increased accuracy as compared with MC codes. These codes produce particle field distributions that agreed with three MC codes (Geant4, FLUKA, PHITS) to the degree that the three MC codes agree among themselves (Wilson et al., 2014a-c). Clearly, the expanded treatment of the interaction cross sections (from straight-ahead to forward/backward to forward/isotropic) and a more complete treatment of the angular dependence would further improve the results.

The next progression was to maintain the quasi–elastic term as the only straight–ahead component and treat the constituent recoil term with the Ranft angular factor while maintaining the evaporation products as isotropic. There were large differences in comparison with MC, and it was surmised that the quasi–elastic component contributed to the discrepancy and needs improvement (Wilson et al., 2017a). This last step prompted a reexamination of the quasi-elastic term and a new approach was identified. An intra-nuclear transport theory (Wilson et al., 1986) was introduced to provide an independent formalism for the quasi-elastic scattering (Wilson et al., 2017b). It was clear that the older ad hoc approach to the quasi-elastic term provided a less than ideal version of nucleon quasi-elastic scattering and provided motivation to develop an even more complete and accurate formalism.

In the present report, we will extend the neutron/light-ion 3D transport beyond the Bertini/Ranft approximation by improving the Serber first step (Serber, 1947) in which a more complete treatment of 3D effects in the 3DHZETRN-v2.1 code is incorporated. Development of the improved Serber is achieved while facilitating convergence studies of differing shield geometries and materials (Wilson et al., 2016; Slaba et al., 2016). In addition to functional changes within the nuclear model, the 3D code has a selectable angular convergence parameter for the lower energy neutrons and light-ions that need broader angular extension. Furthermore, the quasi-elastic/multiple-production model of the quasi-elastic and multiple production terms will be expanded by replacing the Bertini/Ranft multiple-production terms with values from the Serber first step. These advances will use available MC codes, Geant4 (Agostinelli et al., 2003; Geant4 Collaboration, 2012a,b), FLUKA (Fasso et al., 2005; Battistoni et al., 2007), and PHITS (Sato et al., 2006, 2013; Niita et al., 2006), to judge the accuracy of these developments, especially with regard to their 3D aspects. The options in MC usage are discussed in Wilson et al. (2014a,b). Upon completion, the 3DHZETRN-v2.1 code will be validated against spaceflight data, as used in spacecraft design (Verhage et al., 2002), and integrated into the web-based OLTARIS software system (Singleterry et al., 2011) for general testing.

2. Status of 3DHZETRN-v2 Code

The relevant transport equations are the coupled linear Boltzmann equations derived on the basis of conservation principles (Wilson et al., 1977, 1991) for the differential fluence density, $\phi_j(\mathbf{x}, \mathbf{\Omega}, E)$ in units of 1/(MeV-cm^2) of type j particles at position $\mathbf{x}$ (g/cm^2), angle $\mathbf{\Omega}$ in steradians (sr), and kinetic energy, E (MeV/n),

$$\mathbf{B}[\phi_j(\mathbf{x}, \mathbf{\Omega}, E)] = \sum_k \int \sigma_{jk}(\mathbf{\Omega}, \mathbf{\Omega}', E, E')\phi_k(\mathbf{x}, \mathbf{\Omega}', E')d\Omega' dE' - \sigma_j(E)\phi_j(\mathbf{x}, \mathbf{\Omega}, E), \tag{1}$$

where $\mathbf{B}[\phi_j(\mathbf{x}, \mathbf{\Omega}, E)]$ is the Boltzmann transport operator (Wilson et al., 1991, 2005) given as

$$\mathbf{B}[\phi_j(\mathbf{x}, \mathbf{\Omega}, E)] = \mathbf{\Omega} \cdot \nabla \phi_j(\mathbf{x}, \mathbf{\Omega}, E) - A_j^{-1} \frac{\partial}{\partial E}[S_j(E)\phi_j(\mathbf{x}, \mathbf{\Omega}, E)],$$

where $\sigma_j(E)$ is the total macroscopic cross section, $\sigma_{jk}(\mathbf{\Omega}, \mathbf{\Omega}', E, E')$ is the macroscopic double differential cross section evaluated in the medium, and $S_j(E)$ is the stopping power ($S_n(E)$ vanishes for neutrons $j = n$) for particle j of mass A_j. The macroscopic cross section is found by multiplying the microscopic cross section (cm^2) by the number of atoms per gram of the target; $\sigma_{\text{macro}}(E) = \sigma_{\text{micro}}(E)\rho_{\text{targ}}$, where $\rho_{\text{targ}} = N_A/mw$; mw is the molecular weight of the target expressed in units of (g/mol), and N_A is Avogadro's number (atoms/mol). Therefore, the macroscopic cross section has units of cm^2/g, which is consistent with the standard use of the areal density of g/cm^2 for a position vector, $\mathbf{x}$, employed in radiation transport calculations. The double differential cross section, $\sigma_{jk}(\mathbf{\Omega}, \mathbf{\Omega}', E, E')$ in units of cm^2/(g-MeV-sr), describes reactions for which a particle of type k with kinetic energy E' and direction $\mathbf{\Omega}'$ yields a particle of type j with kinetic energy E in direction $\mathbf{\Omega}$.

Equation (1) is subject to a boundary condition over the enclosure of the solution domain. At the present level of development, the double differential interaction cross-sections are approximated by a forward directed quasi-elastic (qe) component, an angular dependent multiple-production (mp) component (Wilson et al., 2017b), and additional evaporative de-excitation and elastic scattering term, which is referred to as remainder (rem):

$$\begin{aligned}\sigma_{jk}(\mathbf{\Omega}, \mathbf{\Omega}', E, E') =& \sigma_{jk,qe}(\mathbf{\Omega}, \mathbf{\Omega}', E, E') + \sigma_{jk,mp}(\mathbf{\Omega}, \mathbf{\Omega}', E, E') + \sigma_{jk,rem}(\mathbf{\Omega}, \mathbf{\Omega}', E, E') \\ =& \sigma_k^{\text{abs}}(E')[F_{jk,qe}(E, E')\delta(\mathbf{\Omega} - \mathbf{\Omega}') + F_{jk,mp}(E, E')g_R(\theta, E, A_T)] \\ &+ \sigma_{jk,rem}(\mathbf{\Omega}, \mathbf{\Omega}', E, E'),\end{aligned} \tag{2}$$

where $\sigma_k^{\text{abs}}(E')$ is the total absorption cross section, and $g_R(\theta, E, A_T)$ is the Ranft (1980) angular factor. The first term of equation (2) represents the quasi-elastic multiply scattered component (to be defined in the next section) that is assumed to travel straight forward with spectrum $F_{jk,qe}(E, E')$. The second term is for those nucleons and other light-ions that result from intra-nuclear collisions of the quasi-elastic scattered primary particles with the target nuclear material and are associated with broadly dispersed lower energy particles produced with spectral distributions $F_{jk,mp}(E, E')g_R(\theta, E, A_T)$. The third term includes target fragments from de-excitation processes and elastic scattering as represented by Chew's impulse approximation (Chew, 1951), a phenomenological S-wave for neutrons that provides an adequate representation of the neutron KERMA (Wilson, 1973; Wilson et al., 1991). (Future improvements are being planned (Werneth et al., 2017). The angular dispersion in the multiple-production term at each energy is taken from the Ranft (1980) angular factor used in early versions of FLUKA:

$$g_R(\theta, E, A_T) = \begin{cases} N_R e^{-\theta^2/\lambda_R}, & 0 \le \theta \le \pi/2 \\ N_R e^{-\pi^2/4\lambda_R}, & \pi/2 < \theta \le \pi. \end{cases} \tag{3}$$

N_R is an energy dependent normalization factor, A_T is the target nuclear mass number, and the Ranft width factor is

$$\lambda_R = (0.12 + 0.00036 A_T)/E, \tag{4}$$

where $\cos\theta = \mathbf{\Omega} \cdot \mathbf{\Omega}'$. Note that the normalization is $\int g_R(\theta, E, A_T) d\Omega = 1$.

In recent work (Wilson et al., 2017b), the Bertini/Ranft quasi-elastic (qe component of equation (2)) term was replaced with results from a Serber nuclear transport model (Serber, 1947) yielding improved results. The nucleonic quasi-elastic differential cross section was found from

$$\sigma_{jk,qe}(E, E') = \frac{2\pi}{\pi R^2} \sigma_k^{abs}(E') f_{jk,qe} \int \phi_{ms}[z(b), E, E'] b db, \tag{5}$$

where $z(b)$ is the target chord at impact parameter $b \ni \{0, R\}$, $f_{jk,qe} = N_{jk,qe} / \sum_l N_{lk,qe}$ is the Bertini/Ranft branching ratio for the quasi-elastic component (Wilson et al., 1988a), and $\phi_{ms}(z, E, E')$ is the spectrum of the multiply-scattered primary nucleon of initial energy E' solution from nuclear transport theory (Wilson et al., 1988a, 2017b).

The second term for multiple-production (mp) in equation (2) represents highly spectrally dispersed particles of lower energy (Wilson, 1977; Wilson et al., 1988a) with energy spectral components given as modifications of Ranft (1980) in the current version of 3DHZETRN-v2 (Wilson et al., 2017a,b) as

$$\sigma_{jk,mp}(E, E') = \sigma_k^{abs}(E') \sum_{i=2}^{3} N_{jk,i} \left(\frac{\alpha_i^{-1} e^{-E/\alpha_i}}{1 - e^{E'/\alpha_i}} \right), \tag{6}$$

where i is related to the Ranft spectral components with spectral parameter α_i (Wilson et al., 1991). A more fundamental formulation of multiple production will be the focus of the present study. The de-excitation spectrum, where $N_{jk,1}$ is the evaporation multiplicity with parameters from the Bertini/Ranft model (Wilson et al., 1988a, 1991), and elastic scattering contributions are included in $\sigma_{jk,rem}$:

$$\sigma_{jk,rem}(\mathbf{\Omega}, \mathbf{\Omega}', E, E') = \sigma_k^{abs}(E') \frac{N_{jk,1}}{4\pi} \left(\frac{\alpha_1^{-1} e^{-E/\alpha_1}}{1 - e^{E'/\alpha_1}} \right) + \sigma_{jk,el}(\mathbf{\Omega}, \mathbf{\Omega}', E, E'). \tag{7}$$

Wilson et al., 2017b found the Bertini/Ranft quasi-elastic term from reference (Wilson et al., 1988a) to be overly simplified and implemented a transport based nuclear interaction model (Wilson et al., 1986) to give a direct estimate of the quasi-elastic spectrum (equation (5)). However, the Bertini cascade multiplicities, branching ratios, and Ranft parameters for the multiple-production term were maintained (Wilson et al., 2016). The resulting improvements in that study encouraged the authors to replace the multiple-production cross-sections in equation (6) with a more fundamental evaluation using the transport nuclear model.

In recent work, the forward and isotropic fractions were arranged into a bi-directional forward/backward transport algorithm with the first order isotropic term treated as a directional dependent perturbation (Wilson et al., 2014a, 2015), which showed improvement over prior bi-directional methods (Clowdsley et al., 2000, 2001; Heinbockel et al., 2003, 2009). In a more recent study, the authors used a straight-ahead approximation for a Serber quasi-elastic term and the Bertini/Ranft multiple-production term of equation (6) as an angular dependent perturbation using equation (3). In the present study, the Bertini/Ranft multiple-production term is replaced with an evaluation of the corresponding multiple-production (target constituent recoil) term using a transport nuclear model (Wilson et al., 1986, 2017b) based on the Serber proposal (Serber, 1947).

3. A Dynamical Theory of the Serber Model

The Serber model has been used to develop stochastic models of nuclear reactions to generate nuclear data for nucleon transport codes (Goldberger, 1948; Metropolis et al., 1958; Bertini, 1969). The Serber model is implemented herein as a linear Boltzmann equation (Wilson et al., 1986, 2017b) derived on the basis of conservation principles for the fluence density of nucleons, $\phi(z, E, E_0)$ (nucleons/fm^2-MeV), moving through nuclear matter with initial energy E_0 at depth $z = 0$ fm to energy E (MeV) given at lowest order as a one dimensional approximation by (Wilson et al., 1986, 2017b)

$$\partial_z \phi(z, E, E_0) + \rho\sigma_m(E)\phi(z, E, E_0) = \int_E^\infty \rho\sigma(E')f_m(E, E')\phi(z, E', E_0)dE'. \tag{8}$$

ρ is the nucleon density within nuclear matter (ρ= 0.1222 fm^{-3}), $\sigma_m(E)$ is the media modified total two-nucleon cross-section, $\sigma(E')$ is the free two-body total cross section, and $f_m(E, E')$ represents the media modified spectrum resulting from processes by which a nucleon with energy E' interacts with nuclear matter and two nucleons emerge from the interaction site with a spectral distribution of energy E (Wilson et al., 2017b). The resulting transport is modified within the region of nuclear media in which the target nucleus is represented by a liquid drop of density ρ (Joos, 1958) with a potential well depth, V_0 (32 MeV). The interior nucleons are distributed in kinetic energy according to the Fermi-Dirac function in phase space up to the Fermi maximum energy of ϵ_F (24.5 MeV), which is the top level of the Fermi sea. The Fermi energy distribution is given as

$$D(\epsilon) = \frac{3}{2\epsilon_F}\sqrt{\frac{\epsilon}{\epsilon_F}}. \tag{9}$$

Hence, the nucleons of the nuclear media are in states of various kinetic energies, $0 < \epsilon < \epsilon_F$, below the binding energy of the least bound nucleon V_B (7.5 MeV). Note that the lowest energy transfers, Δ, given by $\epsilon_F - \epsilon$ are blocked by the Pauli exclusion principle and that collisions on the range of $\epsilon_F - \epsilon < \Delta < V_0$ contribute to nuclear excitation. The solution domain in equation (8) is over $\{\epsilon_F, E_0\}$ where E_0 is the initial energy of the nucleon at $z = 0$. The spectral distribution of the resulting nucleonic field at various locations is evaluated by solving equation (8).

3.1. The Interaction Parameters

The differential cross section of free nucleons for producing a nucleon of energy E from the interaction by a nucleon of energy E' is further discussed in Wilson et al. (1986, 1991) and approximated by the free space isotopic averaged two-nucleon cross sections $\sigma = \frac{1}{2}(\sigma_{pp} + \sigma_{pn})$ as

$$\begin{aligned}
\sigma(E, E') &= \sigma(E')\frac{\left[B(E')e^{-B(E')(E'-E)} + B(E')e^{-B(E')E}\right]}{1 - e^{-B(E')E'}} \\
&= \sigma(E')f(E, E') \\
&= \sigma_e(E, E') + \sigma_r(E, E') \\
&= \sigma(E')[f_e(E, E') + f_r(E, E')] = \sigma_e(E, E') + \sigma_r(E, E')
\end{aligned} \tag{10}$$

where $\sigma(E')$ is the total free two nucleon cross section, $f_e(E, E')$ is the spectrum of the scattered nucleon, and $f_r(E, E')$ is the spectrum of the nucleon recoiling from its "resting" position. The slope parameter $B(E')$ is nearly energy independent above 400 MeV and is approximated by (Wilson et al., 1991)

$$B(E') \approx 2mc^2\ 10^{-6}[3.5 + 40e^{-E'/200}], \tag{11}$$

where mc^2 is the nucleon rest energy (taken as 938 MeV in the current example). Note that the first term is accounting for the elastically scattered spectrum of the incoming nucleon from the struck nucleon, which is labeled as $f_e(E, E')$ in equation (10). The reactive processes are ignored. The $f_e(E, E')$ term dominates for E on the order of the incident energy E'. The second term, labeled as $f_r(E, E')$, provides the spectrum of the target recoil nucleon and dominates the scattering for small E. The free interacting nucleonic cross sections are assumed to be approximately correct in nuclear matter with modifications by nuclear binding (within nuclei) and Pauli exclusion effects. (Additional discussion of nuclear binding effects is summarized by Wilson (1973)). The two-body nucleonic cross sections have been extensively studied and are presented in Fig. 1 (Olive et al., 2014; Werneth et al., 2017). The isotopic averaged cross sections are presently used in equation (10). The two-body cross sections are modified by the Pauli exclusion principle affected by the allowable phase space in nuclear matter. Differential scattering from a free nucleon is given by equation (10), and the total scattering cross section is related to the elastic scattering cross section $\sigma_e(E, E')$ of the projectile as

$$\sigma(E') = \int_0^{E'} \sigma_e(E, E')dE. \tag{12}$$

Note that the $\sigma(E')$ is inversely related to the mean free path, which will be modified since Pauli blocking will restrict the phase space of interaction.

Phase space must be available with the nuclear medium for scattering to occur, and the final states must lie above the Fermi sea, $E > \epsilon_F$. This effect of Pauli blocking is approximated by recognizing that the elastic differential cross section in equation (10) needs modification to account for those regions of phase space that are filled by nuclear matter that are not available under Pauli exclusion. Hence, a Pauli modified differential cross section within the Fermi sea is approximated as

$$\begin{aligned}\sigma_m(E, E') =& \sigma(E')f(E, E')\Theta[E' - (\epsilon_F - \epsilon) - E]\Theta[E - \epsilon_F] \\ =& \sigma(E')f_m(E, E') = \sigma_{em}(E, E') + \sigma_{rm}(E, E'),\end{aligned} \tag{13}$$

where the Θ-functions (unit step functions) are phase space modifications of the spectral distribution, and ϵ is the initial kinetic energy of the nucleon within the Fermi sea. Note that the recoil nucleon must have energy above the Fermi energy, ϵ_F, and the maximum energy of E is $E' - (\epsilon_F - \epsilon)$, where $(\epsilon_F - \epsilon)$ is the energy required to raise the nucleon of nuclear matter of energy ϵ to be above the Fermi sea. The total cross section for interaction with a nucleon of energy ϵ in nuclear matter becomes

$$\begin{aligned}\sigma_m(E') &= \int_0^{E'} \sigma(E')f_e(E, E')\Theta[E' - (\epsilon_F - \epsilon) - E]\Theta[E - \epsilon_F]dE \\ &= \sigma(E') \int_{\epsilon_F}^{E'-(\epsilon_F-\epsilon)} f_{em}(E, E')dE \\ &= \sigma(E') \left[\frac{e^{-B(E')(\epsilon_F-\epsilon)} - e^{-B(E')(E'-\epsilon_F)}}{1 - e^{-B(E')E'}}\right] = \sigma(E')F_P(E', \epsilon).\end{aligned} \tag{14}$$

The Pauli blocking factor for a nuclear constituent of initial energy ϵ is given by the function of the incident energy E' as

$$F_P(E', \epsilon) = \frac{e^{-B(E')(\epsilon_F-\epsilon)} - e^{-B(E')(E'-\epsilon_F)}}{1 - e^{-B(E')E'}}, \tag{15}$$

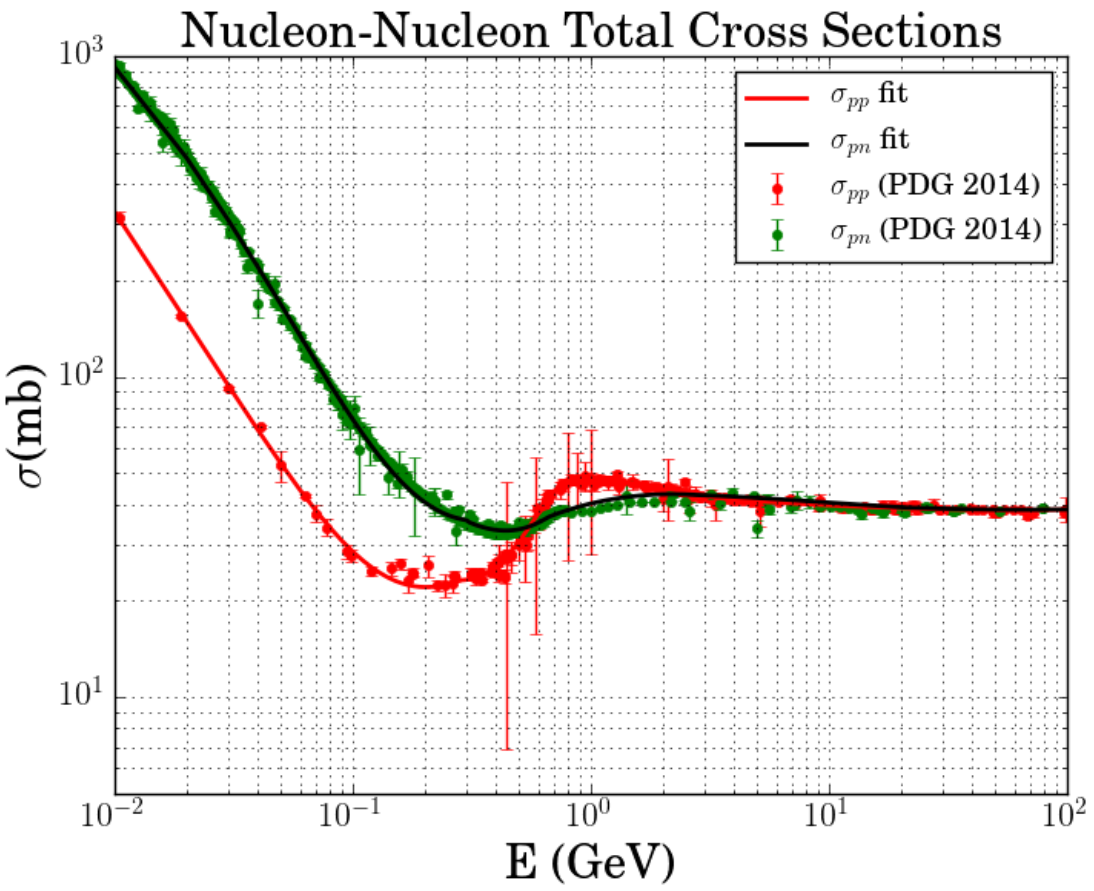

Figure 1: Total nucleonic two-body cross sections (Olive et al., 2014; Werneth et al., 2017) for proton-proton (pp) and proton-neutron (pn) reactions. Experimental data from the Particle Data Group (PDG) are represented with dots and error bars and were extracted from Olive et al. (2014). Fits to the data are taken from Werneth et al. (2017) and are represented by solid lines.

where $F_P(E',\epsilon)$ is valid over the domain of positive values. Thus, $(\epsilon_F-\epsilon)<(E'-\epsilon_F)$ indicates that $E'>\epsilon_F$ and $\epsilon_F>\epsilon$ so that $E'=2\epsilon_F-\epsilon$ is the boundary where the inequalities are satisfied. The fraction of constituent nucleons of nuclear matter with energy ϵ is $D(\epsilon)d\epsilon$, and the average bound nucleon blocking is

$$F_P(E') = \int_{\epsilon_L}^{\epsilon_F} D(\epsilon)d\epsilon \frac{e^{-B(E')(\epsilon_F-\epsilon)} - e^{-B(E')(E'-\epsilon_F)}}{1-e^{-B(E')E'}}$$
$$= \frac{e^{-B(E')\epsilon_F}\sum_{n=0}^{\infty} C_n - C_0 e^{-B(E')(E-\epsilon_F)}}{1-e^{-B(E')E'}}, \tag{16}$$

where

$$C_n = \frac{[B(E')\epsilon_F]^n}{n!(1+\frac{3n}{2})}\left[1-\left(\frac{\epsilon_L}{\epsilon_F}\right)^{n+3/2}\right].$$

The lower limit on the integral over ϵ is then $\epsilon_L=(2\epsilon_F-E')\Theta(2\epsilon_F-E')$. The result is shown in Fig. 2. Also in Fig. 2 for comparison are the semi-empirical values we have used previously (Wilson et al., 1987a,b, 2017b) based on the work of Dymarz and Kohmura (1983). The two-body isotopic averaged cross section, $\sigma(E')$, and the modified cross section, $\sigma_m(E')$, are shown in Fig. 3. Note that blocking results in zero scattering on/below the Fermi surface.

3.2. Solving the Nuclear Transport Equation

The differential operator of equation (8) can be inverted by using an integrating factor of $\mu(z,E)=e^{\rho\sigma_m(E)z}$ to yield a Volterra integral equation that describes the transport process given by

$$\phi(z,E,E_0)=\phi_0(z,E,E_0)+\int_0^z e^{-\rho\sigma_m(E)(z-z')}\int_{\epsilon_L}^{\infty}\rho\sigma_m(E,E')\phi(z',E',E_0)dE'dz' \tag{17}$$

that may be solved as a perturbation series (Lamkin, 1974; Wilson and Lamkin, 1974, 1975; Wilson et al., 1986). The first term consists of the uncollided particle beam as

$$\phi_0(z,E,E_0)=e^{-\rho\sigma_m(E)z}\phi(0,E,E_0), \tag{18}$$

where the boundary condition, $\phi(0,E,E_0)$, is assumed herein to be a mono-energetic beam at the initial energy E_0 so that $\phi(0,E,E_0)=\delta(E-E_0)$, which is the only term of the series solution with $E\geq E_0-(\epsilon_F-\epsilon)$. Higher order corrections can be found by iterating the successive terms, which forms a perturbation series solution of equation (17) where successive terms are given by (Wilson and Lamkin, 1974, 1975)

$$\phi_n(z,E,E_0)=\int_0^z e^{-\rho\sigma_m(E)(z-z')}\int_{\epsilon_L}^{E_0}\rho\sigma_m(E,E')\phi_{n-1}(z',E',E_0)dE'dz', \tag{19}$$

for $E>2\epsilon_F-\epsilon$. Note, $\phi_n(z,E,E_0)$ is null for $E<\epsilon_F$ and $E>E_0-(\epsilon_F-\epsilon)$, where ϵ is the initial energy of the struck nucleon for $n>0$. The lower limit on the energy integral will be labeled as ϵ_L and is equal to E so long as $E>(2\epsilon_F-\epsilon)$, as collisions at lower energies would require scattering into the Fermi sea and are not allowed under the Pauli Principle. The first correction (first perturbation) to the uncollided primary beam term in equation (18) is found by substituting $\phi_0(z,E,E_0)$ into the integral term on the

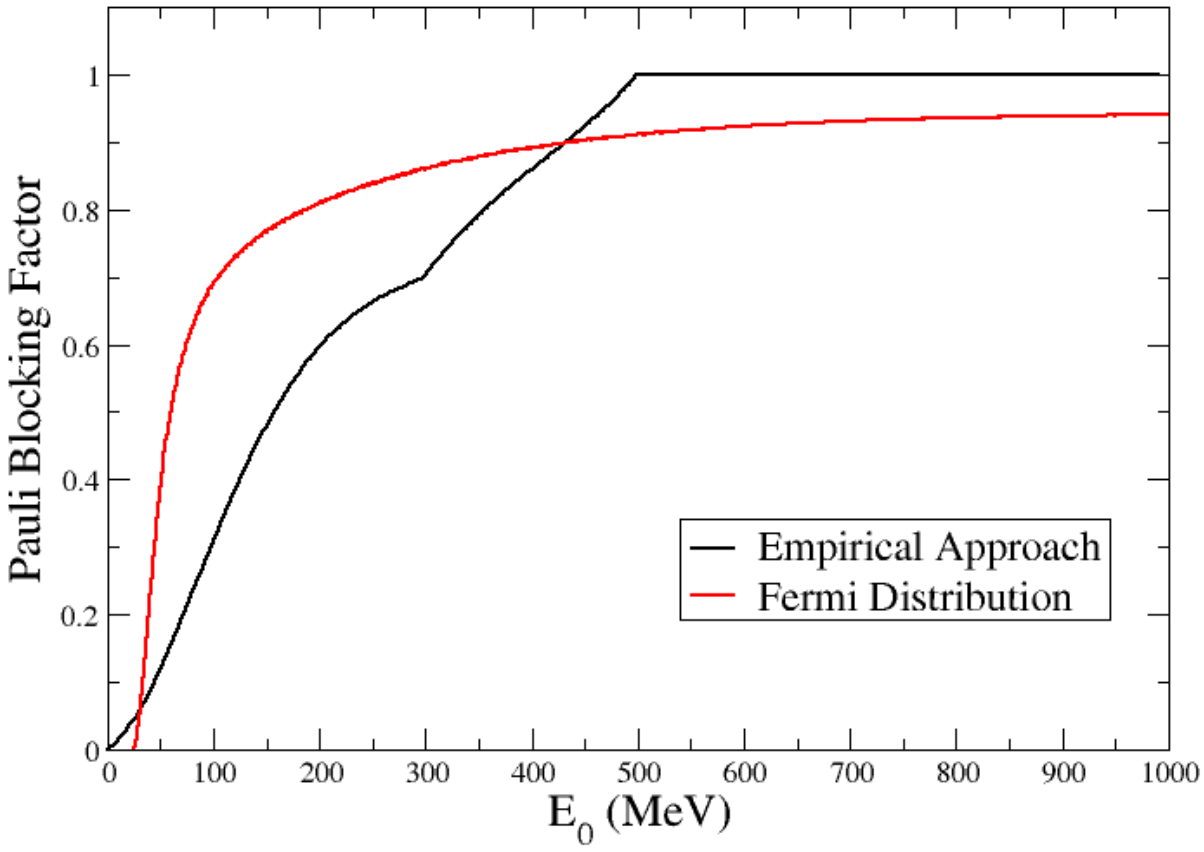

Figure 2: Pauli blocking factor for a nucleon moving through nuclear matter with energy E_0 in the present nuclear model given by equation (16) and empirical values from Wilson et al. (1987a,b) based on Dymarz and Kohmura (1983).

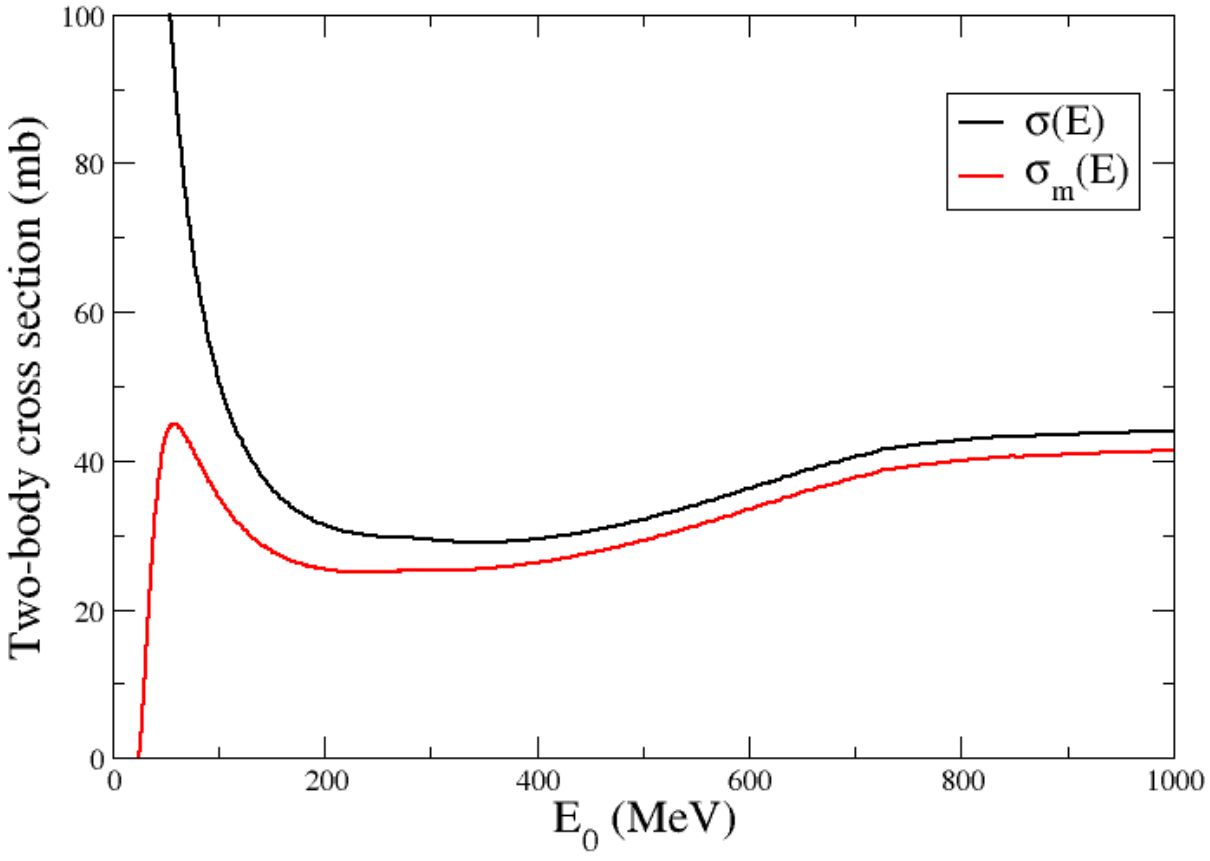

Figure 3: The free two-body cross section (mb) in nuclear matter without the Pauli blocking factor and the Pauli modified cross section as determined by equation (16).

right side of equation (19) as given by

$$\phi_1(z,E,E_0) = \int_0^z e^{-\rho\sigma_m(E)(z-z')} \int_{\epsilon_L}^{E_0} \rho\sigma_m(E,E')\phi_0(z',E',E_0)dE'dz'$$
$$= \left(\frac{e^{-\rho\sigma_m(E)z} - e^{-\rho\sigma_m(E_0)z}}{\rho\sigma_m(E_0) - \rho\sigma_m(E)}\right)\rho\sigma_m(E,E_0), \tag{20}$$

for E on the interval $\{\epsilon_F, E_0 - (\epsilon_F - \epsilon)\}$ as required by the Pauli blocking factor (see equation (13)) and null otherwise. (Note, $\rho\sigma_m(E,E_0)$ contains the factor $\Theta[E_0 - (\epsilon_F - \epsilon)]\Theta[E - \epsilon_F]$.) The fraction of nucleons of nuclear matter with energy ϵ is given by equation (9), and the statistical mean (average over ϵ) of equation (20) is given by

$$\psi_1(z,E,E_0) = \int_{\epsilon_L}^{\epsilon_F} D(\epsilon)d\epsilon\left(\frac{e^{-\rho\sigma_m(E)z} - e^{-\rho\sigma_m(E_0)z}}{\rho\sigma_m(E_0) - \rho\sigma_m(E)}\right)\rho\sigma_m(E,E_0)$$
$$= \left[1 - \left(\frac{\epsilon_L}{\epsilon_F}\right)^{3/2}\right]\left(\frac{e^{-\rho\sigma_m(E)z} - e^{-\rho\sigma_m(E_0)z}}{\rho\sigma_m(E_0) - \rho\sigma_m(E)}\right)\rho\sigma_m(E,E_0). \tag{21}$$

The transition of the step function $\Theta[E_0 - (\epsilon_F - \epsilon) - E]$ occurs at

$$\epsilon_L = E + \epsilon_F - E_0, \tag{22}$$

and provides the lower limit, ϵ_L, for the integral in equation (21), where the upper limit is ϵ_F. Note that ϵ_L is zero when the right side of equation (20) transitions to/from zero, signifying full participation of the constituent nucleons. The $\psi_1(z,E,E_0)$ term describes the spectra of the scattered nucleon contained in the $\sigma_{em}(E,E')$ term in addition to the spectral distribution of the struck nucleon $\sigma_{rm}(E,E_0)$ term. The first scattering of the incident nucleon is then given by the multiply-scattered component of the primary nucleon term of equation (13), $\sigma_{em}(E,E_0)$, as

$$\psi_{s1}(z,E,E_0) = \left[1 - \left(\frac{\epsilon_L}{\epsilon_F}\right)^{3/2}\right]\left(\frac{e^{-\rho\sigma_m(E)z} - e^{-\rho\sigma_m(E_0)z}}{\rho\sigma_m(E_0) - \rho\sigma_m(E)}\right)\rho\sigma_{em}(E,E_0)$$
$$= \left[1 - \left(\frac{\epsilon_L}{\epsilon_F}\right)^{3/2}\right]\left(\frac{e^{-\rho\sigma_m(E)z} - e^{-\rho\sigma_m(E_0)z}}{\rho\sigma_m(E_0) - \rho\sigma_m(E)}\right)$$
$$\times \rho\sigma(E_0)B(E_0)\frac{e^{-B(E_0)(E_0-E)}}{1 - e^{-B(E_0)(E_0)}}, \tag{23}$$

for E on the interval $\{\epsilon_F, E_0\}$ and null otherwise. The notation σ_{em} refers to the quasi-elastic component of σ_m. Similarly, the recoiling nuclear constituent produced by the first scattering is given by the

$\sigma_{rm}(E, E')$ term of equation (13) as

$$\psi_{r1}(z, E, E_0) = \left[1 - \left(\frac{\epsilon_L}{\epsilon_F}\right)^{3/2}\right] \left(\frac{e^{-\rho\sigma_m(E)z} - e^{-\rho\sigma_m(E_0)z}}{\rho\sigma_m(E_0) - \rho\sigma_m(E)}\right) \rho\sigma_{rm}(E, E_0)$$
$$= \left[1 - \left(\frac{\epsilon_L}{\epsilon_F}\right)^{3/2}\right] \left(\frac{e^{-\rho\sigma_m(E)z} - e^{-\rho\sigma_m(E_0)z}}{\rho\sigma_m(E_0) - \rho\sigma_m(E)}\right)$$
$$\times \rho\sigma(E_0)B(E_0)\frac{e^{-B(E_0)E}}{1 - e^{-B(E_0)E_0}} \tag{24}$$

for E on the interval $\{\epsilon_F, E_0\}$ and null otherwise. The graphs of the first quasi-elastic and first recoil terms are shown in Figs. 4 and 5 for several initial energies E_0 of 132, 232, 332, and 432 MeV. Clearly there are higher order terms for both the multiple scattering of the incident nucleon as it moves through the nuclear material and the recoiling nuclear constituents being produced. In these higher order terms, it is assumed that the spectral normalization factor given by $N(E_0) = 1 - e^{-B(E_0)E_0}$ is the same for each additional term evaluation. These assumptions are helpful in evaluation of higher terms and leaves the first scattering event exactly evaluated. The second scattered terms are expected to have slight errors, due to the replacement of $1 - e^{-B(E')E'}$ with $1 - e^{-B(E_0)E_0}$, which increases further in higher order terms (see the Appendix where we demonstrate this error to be somewhat minor). In the following development we describe a small correction that will give an adequate solution for the higher order terms.

3.3. Multiple Scattering Series

To establish the scattering properties of the nuclear media we only evaluate the $\sigma_e(E, E')$ terms in equation (19) for which equation (21) is the lowest order perturbative result. Note, the use of the term "multiple scattering" herein is more limited than we have used elsewhere (Wilson, 1973, 1974, 1975). In the present work, multiply-scattering refers to the scattering of the incident nucleon. We now follow the interactions after the first scattering that generally have further interactions prior to exit through the nuclear boundary. Energy is redistributed after each collision, which affects subsequent collisions. We follow the assumption that $N(E') \approx N(E_0)$ but make a small correction accounting for the redistribution of energy upon scattering by making a slight downshift in the average energy by setting $N(E') = N(\gamma E_0)$, where γ is unity for the first term and $[0.96 - z/200]^{n-1}$ for the nth subsequent terms. The successive multiple scattering terms under the assumptions discussed in the Appendix coupled with these energy corrections leads to

$$\phi_{sn}(z, E, E_0) \approx [\rho\sigma B z]^n [E_0 - (\epsilon_F - \epsilon) - E]^{n-1} \frac{e^{-B(E_0 - E)}}{n!(n-1)!\left[1 - e^{-B\gamma_n E_0}\right]^n}, \tag{25}$$

which is null except when E is on the interval $\{\epsilon_F, E_0 - (\epsilon_F - \epsilon)\}$. Clearly γ is well approximated by $(0.96 - z/200)$. Note that this perturbation approach is similar to the perturbation series (Wilson and Lamkin, 1974, 1975; Lamkin, 1974; Wilson et al., 1986, 2017b). The constituent kinetic energy, ϵ, is distributed according to the Fermi-Dirac theory (see equation (9). Assuming $\sigma_m(E) = \sigma_m(E_0) = \sigma_m$

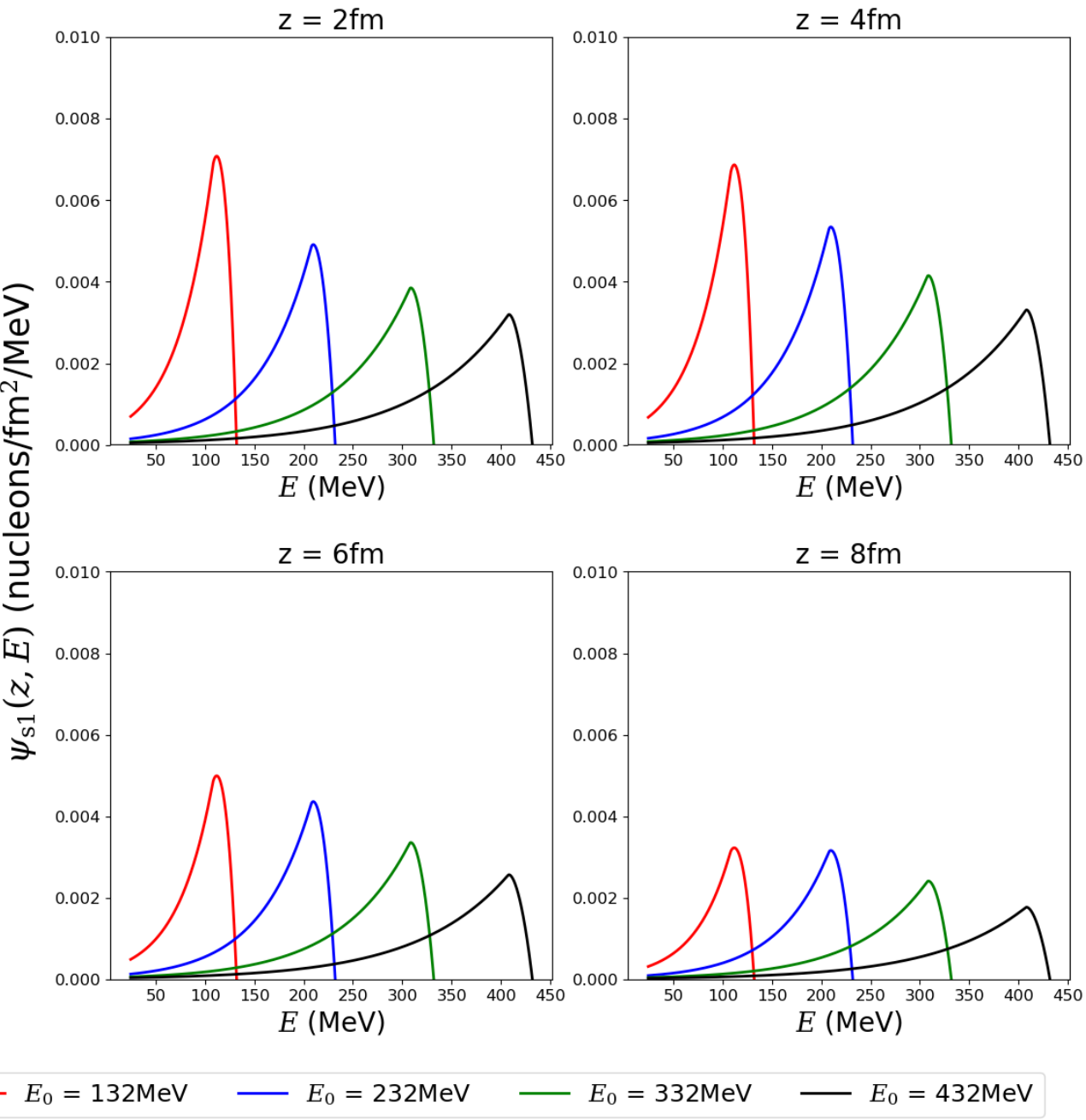

Figure 4: The Pauli blocking effect on the initial scattering of the projectile nucleon at depth z in nuclear matter.

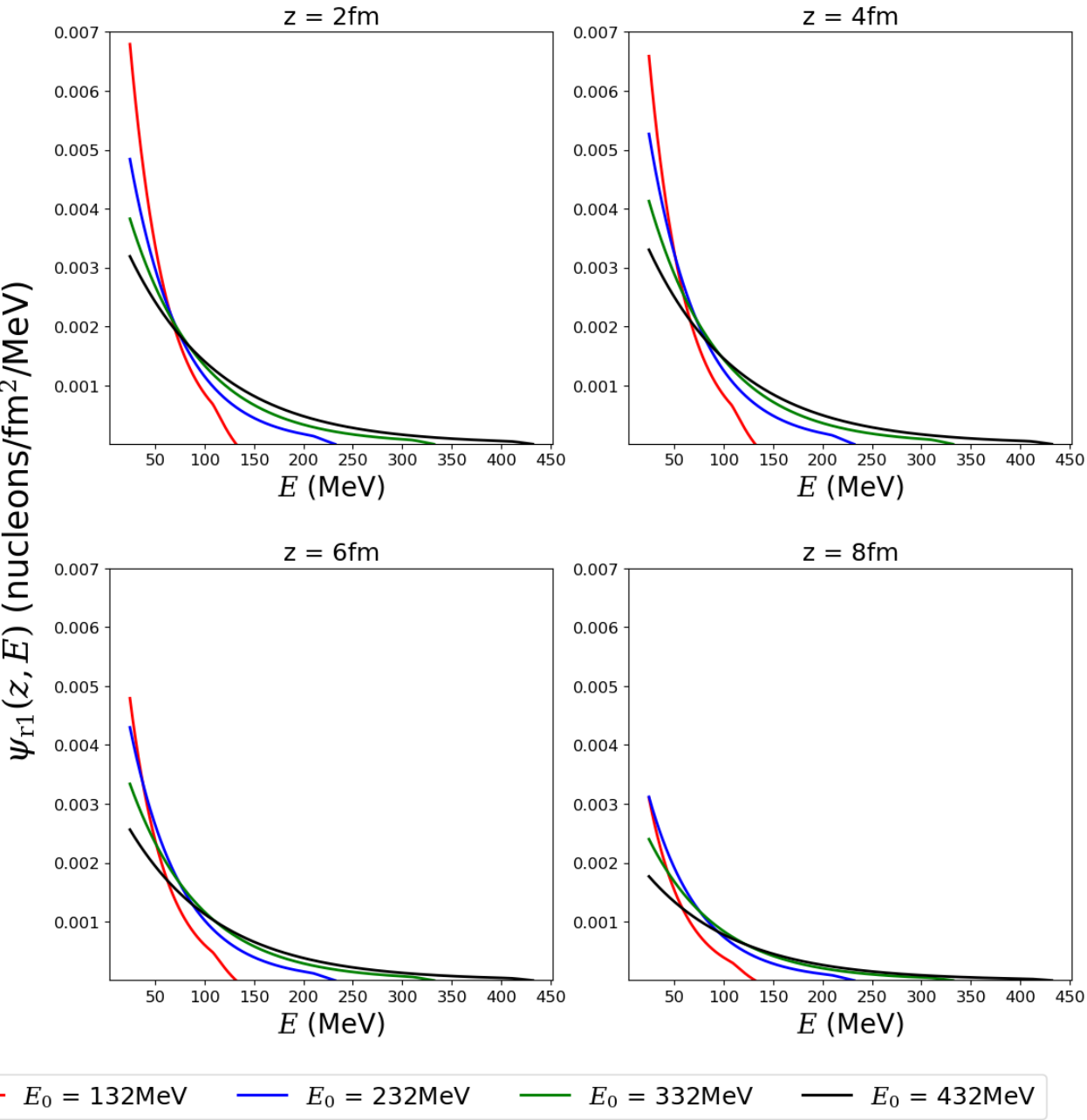

Figure 5: The Pauli blocking effect on the initial recoil of the constituent nucleon at depth z in nuclear matter.

and $B(E) = B(E_0) = B$ results in

$$\begin{aligned}
\psi_{sn} &= \int_{\epsilon_L}^{\epsilon_F} D(\epsilon) d\epsilon \; \phi_{sn}(z, E, E_0) \\
&= \int_{\epsilon_L}^{\epsilon_F} D(\epsilon) d\epsilon \; [\rho\sigma B z]^n [E_0 - (\epsilon_F - \epsilon) - E]^{n-1} \frac{e^{-B(E_0 - E)}}{n!(n-1)! \left[1 - e^{-B\gamma_n E_0}\right]^n} \\
&= [\rho\sigma B z]^n \frac{e^{-\rho\sigma_m z} e^{-B(E_0 - E)}}{n!(n-1)! \left[1 - e^{-B\gamma_n E_0}\right]^n} \int_{\epsilon_L}^{\epsilon_F} D(\epsilon) d\epsilon \, [E_0 - (\epsilon_F - \epsilon) - E]^{n-1} \\
&= [\rho\sigma B z]^n \frac{e^{-\rho\sigma_m z} e^{-B(E_0 - E)}}{n!(n-1)! \left[1 - e^{-B\gamma_n E_0}\right]^n} I_n(E, E_0)
\end{aligned} \tag{26}$$

with the provision that $E > \epsilon_F$ and

$$\begin{aligned}
I_n(E, E_0) = \frac{3}{(2n+1)\epsilon_F^{3/2}} &\left[\epsilon_F^{3/2} (\Delta + \epsilon_F)^{n-1} - \epsilon_L^{3/2} (\Delta + \epsilon_L)^{n-1}\right] \\
&+ \frac{2\Delta(n-1)}{2n+1} I_{n-1}(E, E_0),
\end{aligned} \tag{27}$$

where $\Delta = E_0 - E - \epsilon_F$. The lowest order term ($n = 1$) is given as

$$I_1(E, E_0) = 1 - \left(\frac{\epsilon_L}{\epsilon_F}\right)^{3/2}, \tag{28}$$

which appears in equation (23). In the above, we have described the fate of the incident nucleon and ignored the two nucleonic components, {*p*,*n*}, but the formalism can be extended to include multiple constituents {*p*,*n*} and charge exchange cross sections (Wilson et al., 1991). The complete solution for the scattered nucleon is given as

$$\psi_{ms}(z, E, E_0) = \psi_{s1}(z, E, E_0) + \psi_{s2}(z, E, E_0) + \psi_{s3}(z, E, E_0) + \ldots . \tag{29}$$

The full multiple scattering fluence is shown in Fig. 6. Note that the $\psi_0(z, E, E_0)$ term is the transmitted incident fluence that results from survival without nuclear interaction contributing to nuclear elastic scattering (but without the important diffractive components of the usual quantum multiple scattering series (Wilson, 1974)) and is not part of the present form of the multiple scattering (ms). Furthermore, the ms multiplicity according to results of equations (26) and (29) is given by

$$M_{ms}(z, E_0) = \int_{\epsilon_F}^{E_0} \psi_{ms}(z, E, E_0) dE, \tag{30}$$

where we have used $\psi_{ms}(z, E, E_0)$ given by equation (29). The total differential fluence is then

$$\psi_S(z, E, E_0) = \psi_0(z, E, E_0) + \psi_{ms}(z, E, E_0), \tag{31}$$

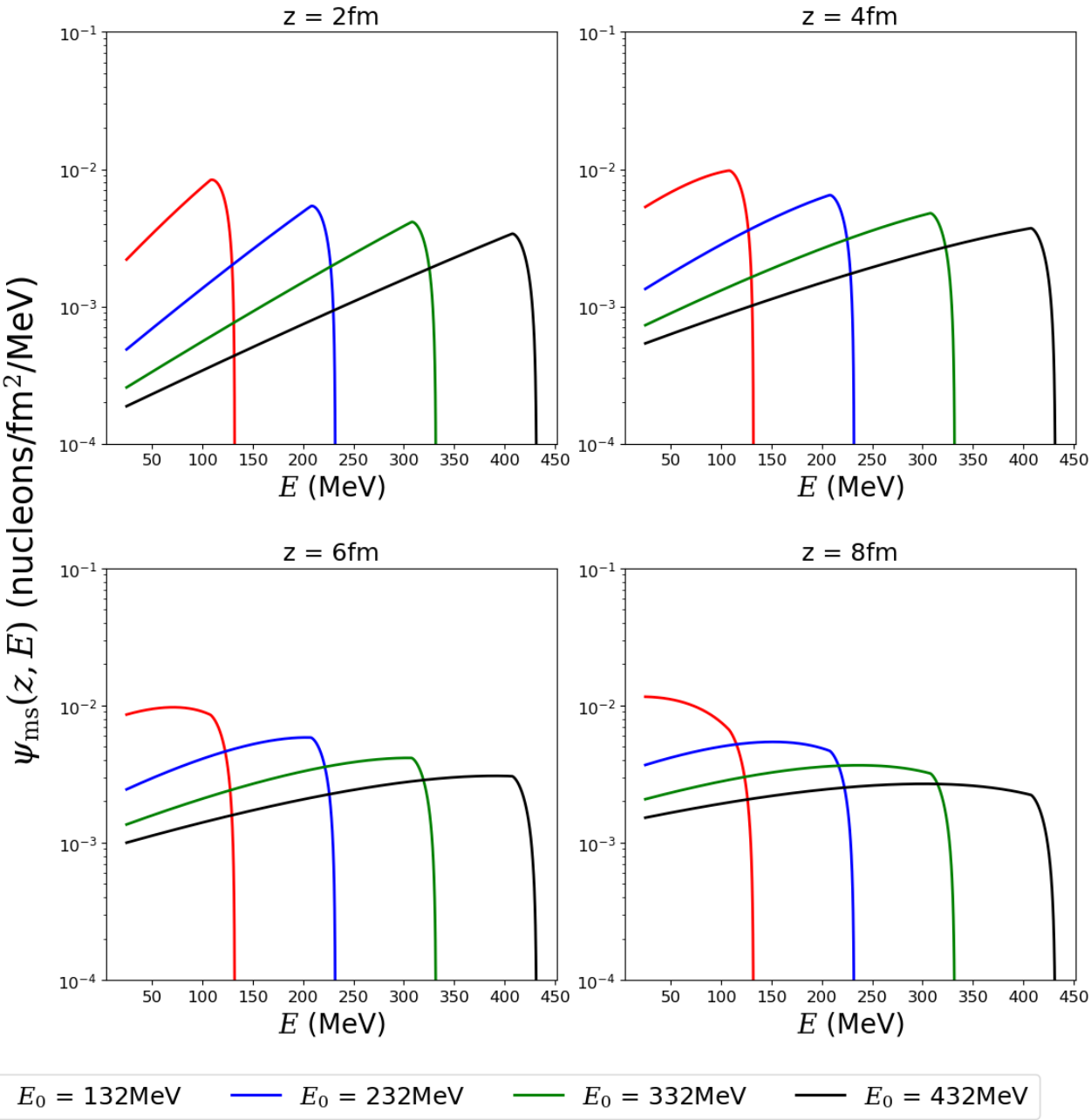

Figure 6: The Pauli blocking effect on the multiple scattering of the projectile nucleon at depth z in nuclear matter.

and the Boltzmann equation must conserve the total fluence as

$$\int_{\epsilon_F}^{E_0} \psi_S(z,E,E_0)dE = 1 = \int_{\epsilon_F}^{E_0} \psi_0(z,E,E_0)dE + \int_{\epsilon_F}^{E_0} \psi_{ms}(z,E,E_0)dE. \tag{32}$$

Thus, the multiple scattered multiplicity is related to the incident fluence and the surviving incident nucleon as

$$\int_{\epsilon_F}^{E_0} \psi_{ms}(z,E,E_0)dE \approx 1 - e^{-\rho\sigma_m(E_0)z} \equiv M_{ms}(z,E_0), \tag{33}$$

where $M_{ms}(z,E_0)$ in equation (33) is the correct (physically required) total multiplicity of multiply scattered nucleons at depth z, and $M_{ms}(z,E_0)$ of equation (30) is the multiplicity associated with the approximate ms solution discussed above (see the Appendix) but with the added γ_n correction as discussed. The integral over dE only has non-zero contributions on the interval $\{\epsilon_F, E_0\}$. The theoretical multiplicity from equation (33) is compared to the approximate multiplicity from equation (30), and examples of spectral errors are provided in the Appendix. The errors in $M_{ms}(z,E_0)$ are generally less than 6 percent difference for energies and penetration depths of current interest. It is clear from the Appendix that the errors are small for the most important spectral components near the incident energy at even large penetration depths as governed by the cross section $\sigma_e(E,E_0)$. At the higher penetration depths, the energy further degrades because of the higher number of collisions. Note that the limitation for E on the interval $\{\epsilon_F, E_0\}$ is clearly apparent in Fig. 6 as observed with the low-energy gap for $E < \epsilon_F$ and the high-energy roll-off for $E_0 - \epsilon_F < E < E_0$. Fewer constituent nucleons at the top of the Fermi sea generally contribute to the scattered fluence as $E \to E_0$; eventually, Pauli exclusion precludes constituent contributions and the fluence spectra falls to zero. We will subsequently discuss the inclusion of these results in the description of the nuclear reactions. In application, equation (29) will only require the branching ratios of the nucleonic component. In the present work, the branching ratios from the Bertini/Ranft model are used (Wilson et al., 1988b).

3.4. Multiple Recoil Series

Next, the multiple recoil series is obtained by employing a methodology that is analogous to the multiple scattering series derivation. The first constituent recoil term results from collision of the initial nucleon of energy E_0, as given by the recoil component of σ_m term of equation (21), which is labeled herein as $\sigma_{rm}(E,E_0)$. The energy of the recoiling nucleons is low and peaked at energies just above the Fermi energy ϵ_F but declines at higher energies as $e^{-B(E_0)E}$. Subsequent recoils produced by these recoiling nucleons decline even more rapidly (Clowdsley et al., 2000) as approximately $e^{-nB(E_0)E}$ with diminished contributions to the recoil spectra (but as one can demonstrate, they make important contributions to nuclear excitation).

The main recoil terms are those produced by interaction of the multiply-scattered incident nucleon with constituents of energy ϵ providing a contribution to the multiple recoil series (Wilson et al., 1986). Assuming $\sigma_m(E) \approx \sigma_m(E_0) \equiv \sigma_m$ and $B(E) = B(E_0) = B$ as before, the results are approximately given by

$$\phi_{rn}(z,E,E_0) = \int_0^z e^{-\rho\sigma_m(z-z')} \int_E^{E_0-(\epsilon_F-\epsilon)} \frac{\rho\sigma_m B e^{-BE}}{1-e^{-B\gamma_n E_0}} \phi_{sn-1}(z',E',E_0)dE'dz', \tag{34}$$

where the $\phi_{sn-1}(z,E,E_0)$ are the prior terms of the multiple scattering series as given in equation (25). Equation (34) represents the recoiling constituent nucleon from the collision of the scattered primary nucleon. All other recoil terms are neglected as being inferior to results from equation (34) (Wilson et al.,

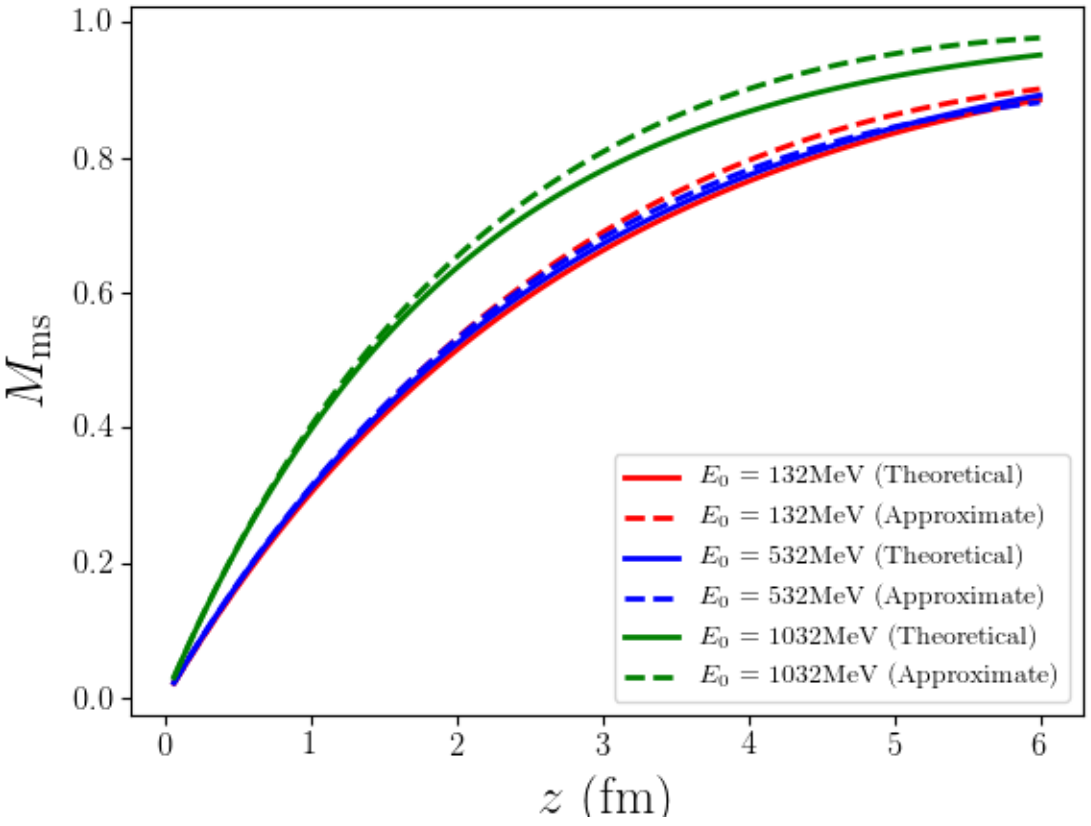

Figure 7: The theoretically correct multiplicity compared to that obtained from the corrected spectral distributions for E_0 of 132, 532 and 1032 MeV as a function of penetration depth z (fm).

1986). Results in equation (34) produce the largest cross terms in the series solutions of the cross terms between $\sigma_e(E, E')$ and $\sigma_r(E, E')$. The first multiple recoil term is given exactly from equation (20) by

$$\phi_{r1}(z, E, E_0) = \rho\sigma z B e^{-\rho\sigma_m z} \frac{e^{-BE}}{1 - e^{-BE_0}}, \tag{35}$$

and the higher order terms can be evaluated analytically under present approximations. The result is

$$\phi_{rn}(z, E, E_0) = [\rho\sigma z]^n e^{-\rho\sigma_m z} B e^{-B(E+\epsilon_F-\epsilon)} \left[\frac{\hat{a}_{n-2}[E_0 - (\epsilon_F - \epsilon) - E]}{n!(n-2)! \left[1 - e^{-B\gamma_n E_0}\right]^n} \right] \tag{36}$$

for E on the interval $\{\epsilon_F, E_0 - (\epsilon_F - \epsilon)\}$ and null otherwise. $\hat{a}_n(t)$ are special functions used in the nucleon-nucleus model by Wilson et al. (1986) and have recurrence relations given by

$$\hat{a}_n(t) = n\hat{a}_{n-1}(t) - t^n e^{-t}, \tag{37}$$

with

$$\hat{a}_0(t) = 1 - e^{-t}. \tag{38}$$

Treating the constituent kinetic energy, ϵ, as distributed according to the Fermi-Dirac theory (see equation (9)) results in

$$\begin{aligned} \psi_{rn}(z, E, E_0) &= \int_{\epsilon_L}^{\epsilon_F} D(\epsilon) d\epsilon \; \phi_{rn}(z, E, E_0) \\ &\approx \left[1 - \left(\frac{\epsilon_L}{\epsilon_F}\right)^{3/2}\right] (\rho\sigma z)^n e^{-\rho\sigma_m z} B e^{-BE} \frac{\hat{a}_{n-2}[B(E_0 - E)]}{n!(n-2)! \left[1 - e^{-B\gamma_n E_0}\right]^n}. \end{aligned} \tag{39}$$

The total approximate recoil fluence is

$$\psi_{mr} = \psi_{r1}(z, E, E_0) + \psi_{r2}(z, E, E_0) + \psi_{r3}(z, E, E_0) \cdots, \tag{40}$$

as shown in Fig. 8. The multiple recoil multiplicity is given as

$$M_{mr}(z, E, E_0) = \int_{\epsilon_F}^{E_0} \psi_{mr}(z, E, E_0) dE. \tag{41}$$

$M_{mr}(z, E_0)$ is the total nucleon recoil fluence at penetration depth z according to equation (41) as shown in Fig. 9. Note that the limitation for E on the interval $\{\epsilon_F, E_0\}$ is seen in the figure by the low-energy gap for $E < \epsilon_F$ and the high-energy roll-off for $E > E_0 - \epsilon_F$. Unlike the ms series, where the multiplicity is given by conservation principles as shown in equation (33), there is no simple method of evaluating the multiple recoil multiplicity as given by equation (41). Application of equation (41) will rely on the Bertini/Ranft model multiplicities and the mr nucleon spectra when applied to a specific nucleus.

3.5. Nuclear Binding Effects

In the above analysis, we have developed a theoretical treatment of interacting nucleons of initial energy E_0 in nuclear media that includes Pauli exclusion effects appropriate to a Fermi gas as the core of the nuclear model, but, thus far, nuclear binding effects have been ignored. Within the region of nuclear matter, the target nucleus is represented by a liquid drop model with a potential well depth of V_0 (≈ 32 MeV) and a Fermi energy of ϵ_F (≈ 24.5 MeV) that is the top level of the Fermi sea below the binding

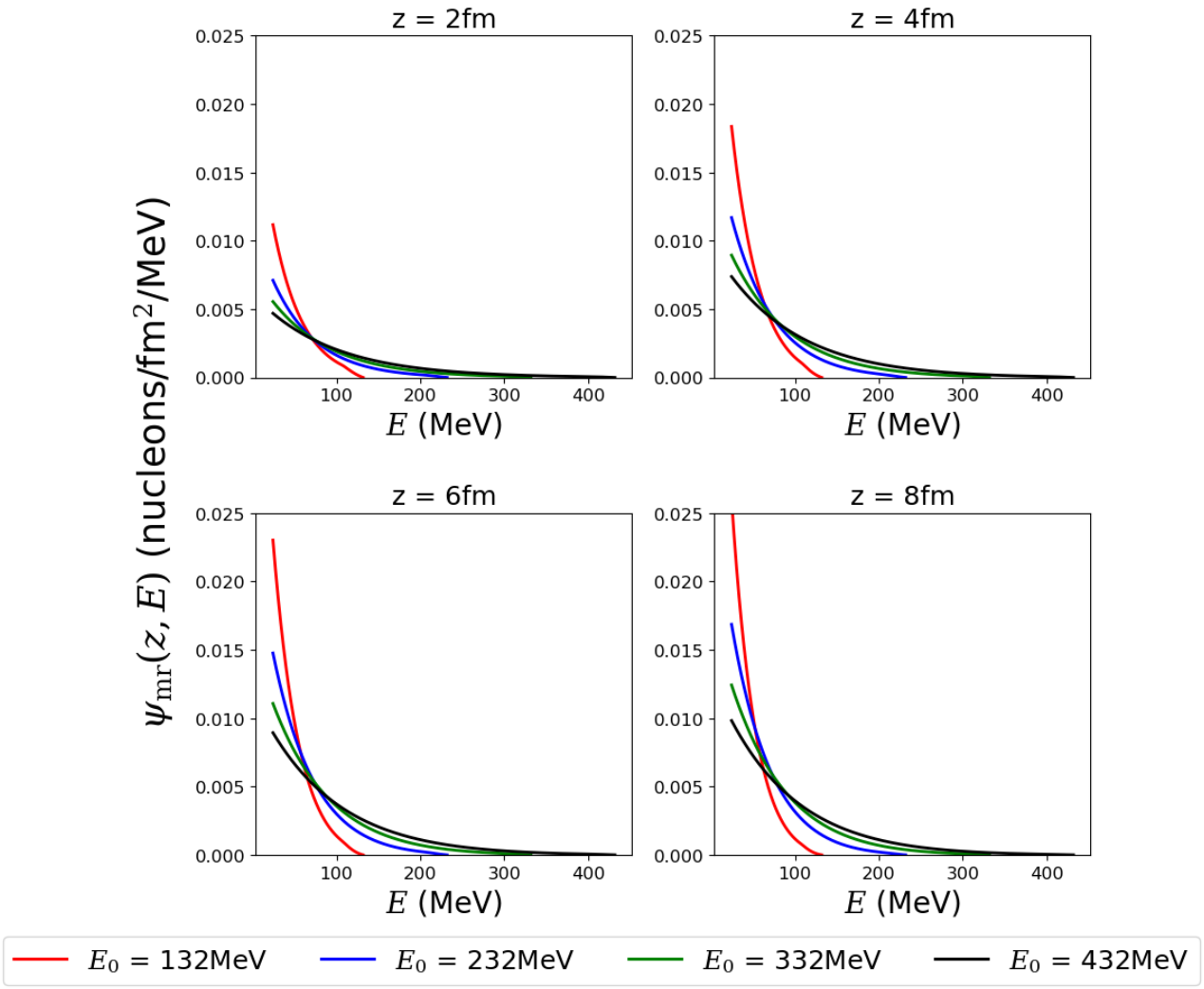

Figure 8: The approximate multiple recoil spectra at various initial energies and depths, z, in nuclear matter using equation (41).

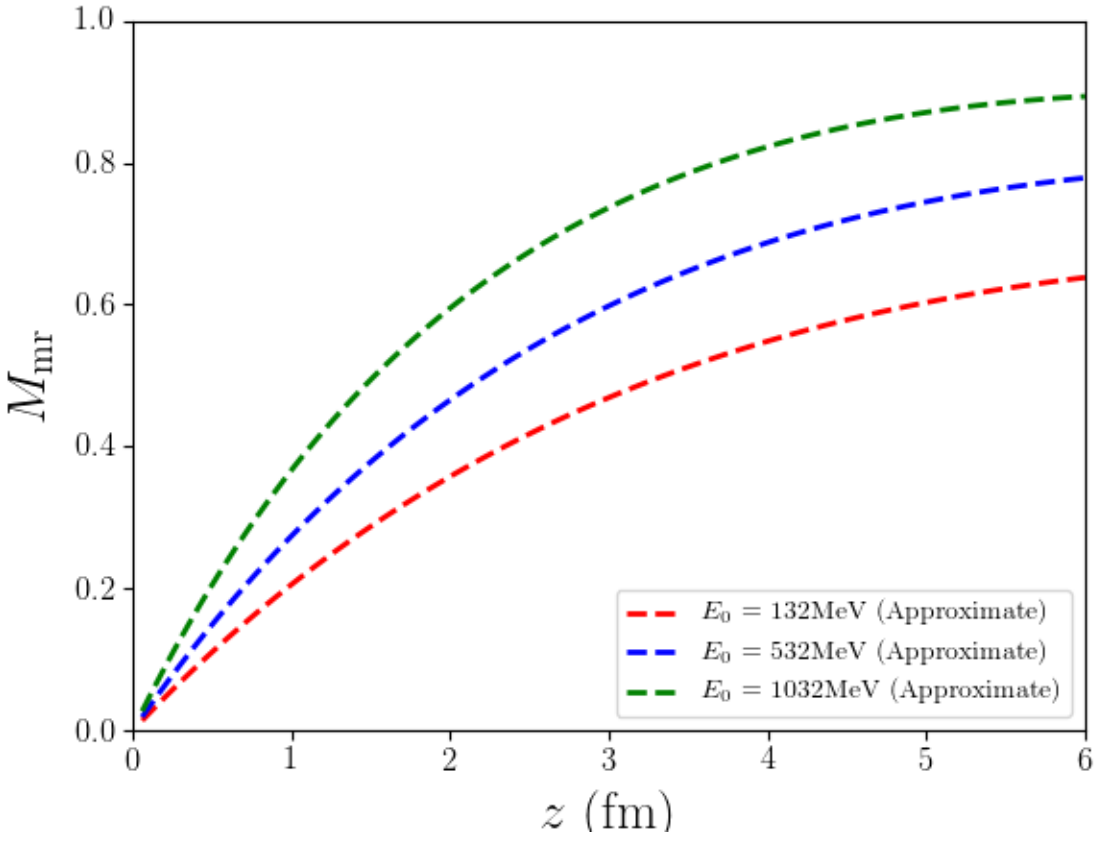

Figure 9: The recoil multiplicity of equation (41) for E_0 of 132, 532 and 1032 MeV as a function of penetration z (fm).

energy of the least bound nucleon V_b ($\approx$ 7.5 MeV) (Joos, 1958). Upon entering the region of the bound nucleons, a nucleon of initial energy, E_L, in the nuclear rest frame (laboratory) is accelerated across the nuclear boundary by the nuclear binding potential well of depth 32 MeV so that its energy on entrance to the nuclear domain is $E_0 = E_L + V_0$. Nucleons within the nuclear domain of energy E experience deceleration upon crossing the nuclear boundary to a final energy in the laboratory of $E_F = E - V_0$ after exiting the nucleus.

Although the energy shifts at each boundary, the fluence in crossing the boundary is conserved. As a result of the energy increase on entrance to the nuclear volume, the net effect on the two-nucleon cross sections within nuclear matter is to effectively shift the interaction energy to higher values, as shown in Fig. 10, resulting from a shift in energy by V_0 (e.g., compare Fig. 10 with Fig. 3).

A second effect is that nucleons with E below V_0 are reflected at the nuclear boundary and trapped within the nuclear volume, which adds to the excitation energy of the nucleus. A useful quantity in this respect is the sticking factor, which is found by using equation (29)

$$S_{FS}(z, E_L) = \int_{\epsilon_F}^{V_0} \psi_{ms}(z, E, E_L + V_0) dE. \tag{42}$$

This is the total number of the nucleons at depth z that contribute to the excitation energy (which will be communicated in a subsequent manuscript). The recoil nucleons are likewise distributed in energy according to equation (40). The nucleons with recoil fluence energy below V_0 are also trapped within the nucleus as

$$S_{FR}(z, E_L) = \int_{\epsilon_F}^{V_0} \psi_{mr}(z, E, E_L + V_0) dE \tag{43}$$

and add to the nuclear excitation energy. The sticking factors for multiple scattering (S_{FS}) and multiple recoil (S_{FR}) are shown in Fig. 11. As expected, the sticking factors generally decrease with increasing laboratory energy. The multiple scattering sticking factor increases with increasing depth as the moderation of the incident nucleon is more complete. A sizable fraction of the multiple recoil energy is committed to nuclear excitation, as expected.

3.6. Connection to the Nuclear Model

Integration of the above formalism into a nuclear model is discussed next. The separation into multiple-scattered and multiple-recoil components will allow us to connect to the projectile and target participants. Spectra given by equations (29) and (40) will be used to evaluate the nucleon spectra from nucleon induced reactions in nuclei. In this evaluation, $\psi_{ms}(z, E, E_0)$ and $\psi_{mr}(z, E, E_0)$ are solutions to the transport of a nucleon in the nuclear media with initial energy E_0 leading to spectral modification by collisions with the media. In the present form of the theory, $\psi_{ms}(z, E, E_0)$ is accurately evaluated, and only branching ratios in relation to the cross sections are required. After traveling a distance z, the mono-energetic spectrum is modified to a spectrum of energy $\psi_{ms}(z, E, E_0)$ and produces a fluence of recoiling nucleons given by $\psi_{mr}(z, E, E_0)$ (that is the dominant solution with other terms neglected). Within the media, the energy, E, takes on values above the top of the Fermi sea, ϵ_F, but nucleons with $E < V_0$ are trapped within the nuclear domain. The quasi-elastic differential spectral distributions, $F_{jk,qe}(E_F, E_L)$, of energy E_F (varies from 0 to E_L) are found with the fluence of equation (29) at each impact parameter averaged over the impact plane as

$$F_{jk,qe}(E_F, E_L) \equiv \frac{2\pi}{\pi R^2} f_{jk,qe} \int \psi_{ms}[z(b), E_F + V_0, E_L + V_0] b db. \tag{44}$$

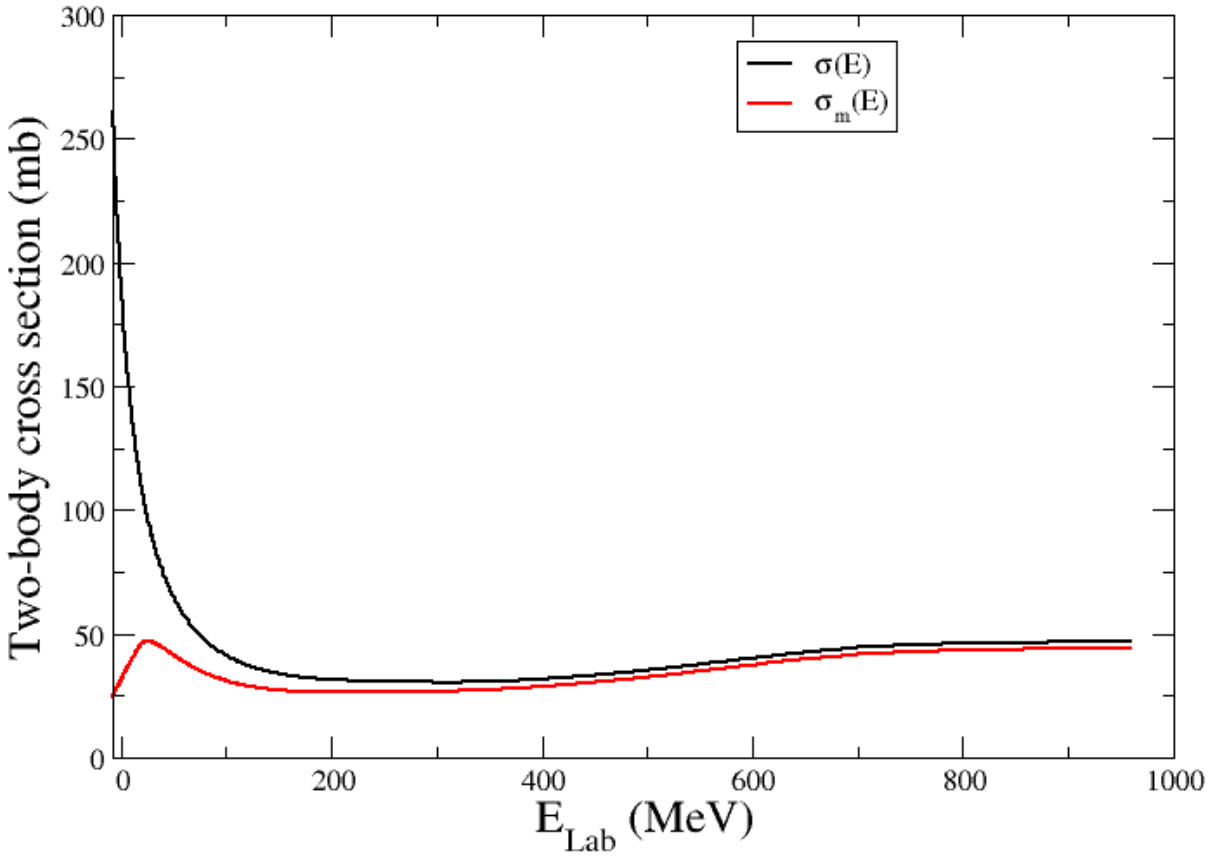

Figure 10: The binding modified free cross section, $\sigma(E)$, and binding Pauli modified cross section, $\sigma_m(E)$, within a nucleus as a function of laboratory energy E_L ($V_0 = 32$ MeV).

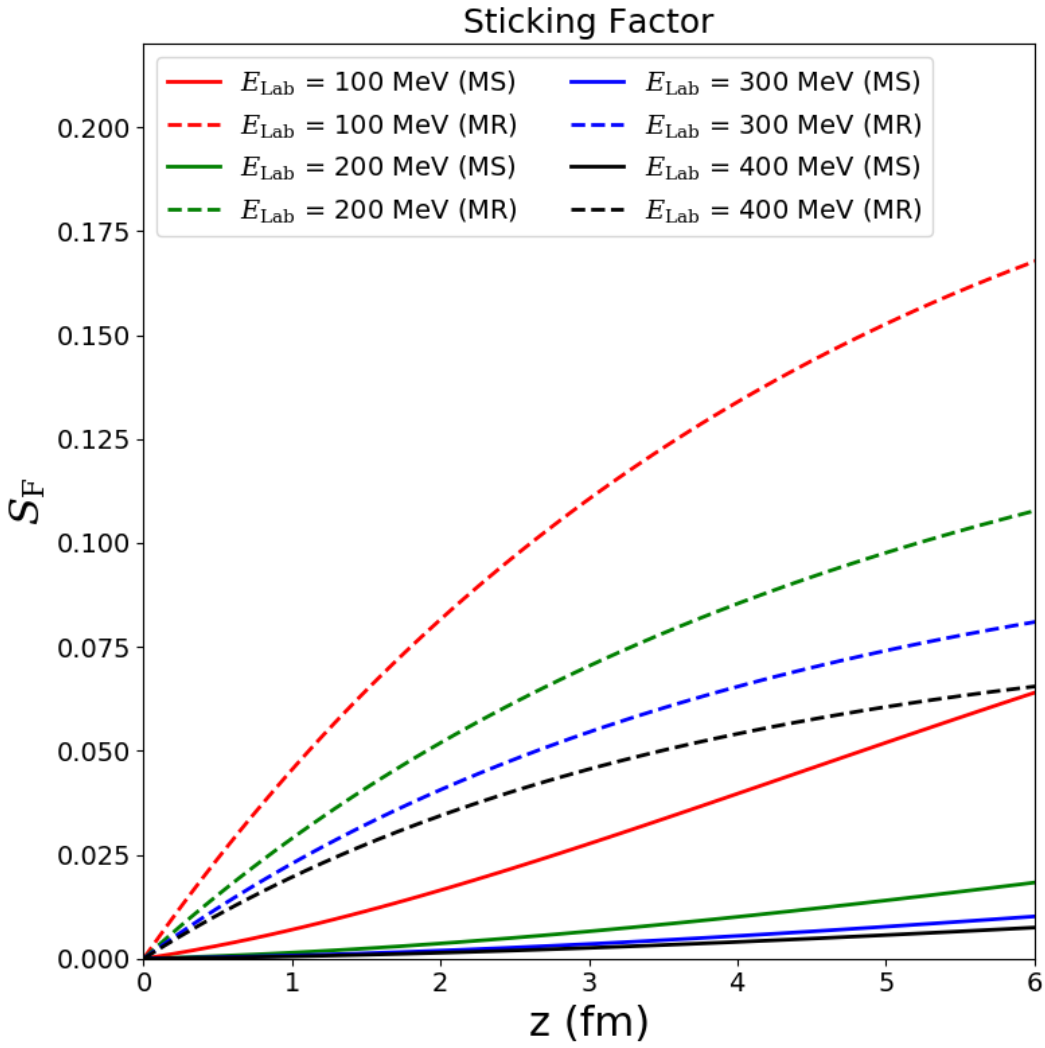

Figure 11: Multiple scattering and multiple recoil sticking factors as a function of penetration depth for four values of laboratory energies of 100, 200, 300, and 400 MeV.

$f_{jk,qe} = N_{jk,qe}/\sum_l N_{lk,qe}$ are the Bertini/Ranft quasi-elastic branching ratios for energy E_L and $z(b)$ is the chord at impact parameter b (Wilson et al., 1986, 2017a). For simplicity, uniform nuclear spherical densities are used (consistent with the liquid drop model).

Noting the less accurate evaluation of $\phi_{mr}(z, E, E_0)$, it is assumed that the dominant term best describes the spectrum of recoils but underestimates the mr multiplicity. The nucleon recoil multiplicities of the exiting nucleons as given by the Bertini/Ranft formalism (Wilson et al., 1988b) are utilized. The multiple-production spectra per exiting nucleon, $F_{jk,mp}(E_F, E_L)$, are found with the Bertini/Ranft multiple-production multiplicity, $N_{jk,mp}$, as

$$F_{jk,mp}(E_F, E_L) \equiv N_{jk,mp} \frac{\int \psi_{mr}[z(b), E_F + V_0, E_L + V_0] bdb}{\int \{M_{mr}[z(b), E_L + V_0] - S_{FR}[z(b), E_L]\} bdb}, \tag{45}$$

where the $N_{jk,mp}$ are the "multiple production" multiplicities at energy E_L of the Bertini/Ranft model and are related to equation (6) by

$$N_{jk,mp} = \sum_{i=2}^{3} N_{jk,i}. \tag{46}$$

This asymmetrical treatment of multiple recoil relative to multiple scattering (compare equations (44) and (45)) results because not all of the recoil terms are evaluated in the present treatment (only the dominant term), which requires an absolute number of recoils to be used. The multiple scattering, however, includes all terms that are known (to within 6 percent or better) and provides an accurate representation of the multiple scattering multiplicity as seen in Fig. 7.

In the above, $R = 1.29a_A$ is the radius (fm) of the equivalent nuclear sphere appropriate to the liquid drop model (Wilson, 1975; Wilson and Costner, 1975). The RMS radius determines the differential scattering cross-section dependence providing the model independent spectral shape at low momentum transfers. The root mean square (RMS) radius a_A is found from the RMS charge radius a_c given in Table 1 by $a_A = \sqrt{a_c^2 - 0.64}$.

Table 1: Root mean square nuclear charge radius a_c (fm) for a nucleus of mass A (Hofstadter and Collard, 1967).

A	a_c
1	0.84
2	2.17
3	1.78
4	1.63
$6 \leq A \leq 14$	2.4
$A > 14$	0.58 + 0.82 $A^{1/3}$

In this context, we will use the quasi-elastic cross section given by

$$\sigma_{jk,qe}(E_F, E_L) = \sigma_k^{abs}(E_L) F_{jk,qe}(E_F, E_L), \tag{47}$$

where $\sigma_k^{abs}(E_L)$ are the accurate total absorption cross sections of Tripathi et al. (1997, 1998, 1999,

2002). Similarly, the multiple production cross sections become

$$\sigma_{jk,mp}(E_F, E_L) = \sigma_k^{abs}(E_L) F_{jk,mp}(E_F, E_L), \tag{48}$$

which will be added to the evaporative de-excitation (see equation (7))

$$F_{jk,evap}(E_F, E_L) = \frac{N_{jk,1}}{\alpha_1} \left(\frac{e^{-\frac{E_F}{\alpha_1}}}{1 - e^{-\frac{E_L}{\alpha_1}}} \right). \tag{49}$$

The Ranft energy parameters are taken from Wilson et al. (1988a,b, 1991). The related evaporative cross section is

$$\sigma_{jk,evap}(E_F, E_L) = \sigma_k^{abs}(E_L) F_{jk,evap}(E_F, E_L), \tag{50}$$

and is assumed to be isotropic. (Note $1/4\pi$ converts equation (50) to angular units.) The fragment spectrum is obtained by summing equations (47), (48), and (50). Each of the model outputs (PHITS, Geant4-Bertini, Geant4-INCL, Bertini/Ranft, and Serber) was normalized to unity so that the differences in spectral shape could be studied. For this reason, the units are 1/MeV instead of mb/MeV.

In the following, equations (47) through (50) will be used as cross sections in light-ion/neutron transport in tissue or shielding materials. For comparison with prior models, the quasi-elastic, multiple-production, and evaporative cross sections were added. As an example, we show the E_L =300 MeV proton-aluminum cross sections for producing neutrons with the present results and compare to other models in Fig. 12. Understanding differences in cross sections of various models, including the MC codes as addressed in Fig. 12, will be helpful in relating differences in transported fluence evaluations from the MC codes and earlier versions of 3DHZETRN. Transport code convergence will be measured using variance techniques on transported fluence results from various codes and nuclear models in the next section.

4. Implementation into the 3DHZETRN-v2 Code

The connection of equations (47) through (50) to 3DHZETRN-v2 is through the double differential cross sections given as

$$\sigma_{jk}(\mathbf{\Omega}, \mathbf{\Omega}', E, E') = \sigma_{jk,qe}(\mathbf{\Omega}, \mathbf{\Omega}', E, E') + \sigma_{jk,mp}(\mathbf{\Omega}, \mathbf{\Omega}', E, E') + \sigma_{jk,rem}(\mathbf{\Omega}, \mathbf{\Omega}', E, E'), \tag{51}$$

where the "quasi-elastic term", $\sigma_{jk,qe}(\mathbf{\Omega}, \mathbf{\Omega}', E, E')$, is related to equation (47), and the "multiple-production term", $\sigma_{jk,mp}(\mathbf{\Omega}, \mathbf{\Omega}', E, E')$, is related to equation (48). The last term of equation (51) includes the evaporation as described by the Bertini/Ranft model and the elastic scattering contribution that was discussed in connection with equation (7). Implementation into 3DHZETRN-v2 assumes the quasi-elastic term is well approximated by the straight-ahead approximation,

$$\sigma_{jk,qe}(\mathbf{\Omega}, \mathbf{\Omega}', E, E') = \delta(\mathbf{\Omega} - \mathbf{\Omega}') \sigma_{jk,qe}(E, E'), \tag{52}$$

and the multiple production term is given as,

$$\sigma_{jk,mp}(\mathbf{\Omega}, \mathbf{\Omega}', E, E') = g_R(\theta, E, A_T) \sigma_{jk,mp}(E, E'), \tag{53}$$

with the energy spectral functions given by equations (47) through (50). The resulting code will be labeled 3DHZETRN-v2.1 and utilizes the prior developments of Slaba et al. (2010, 2013, 2016, 2017).

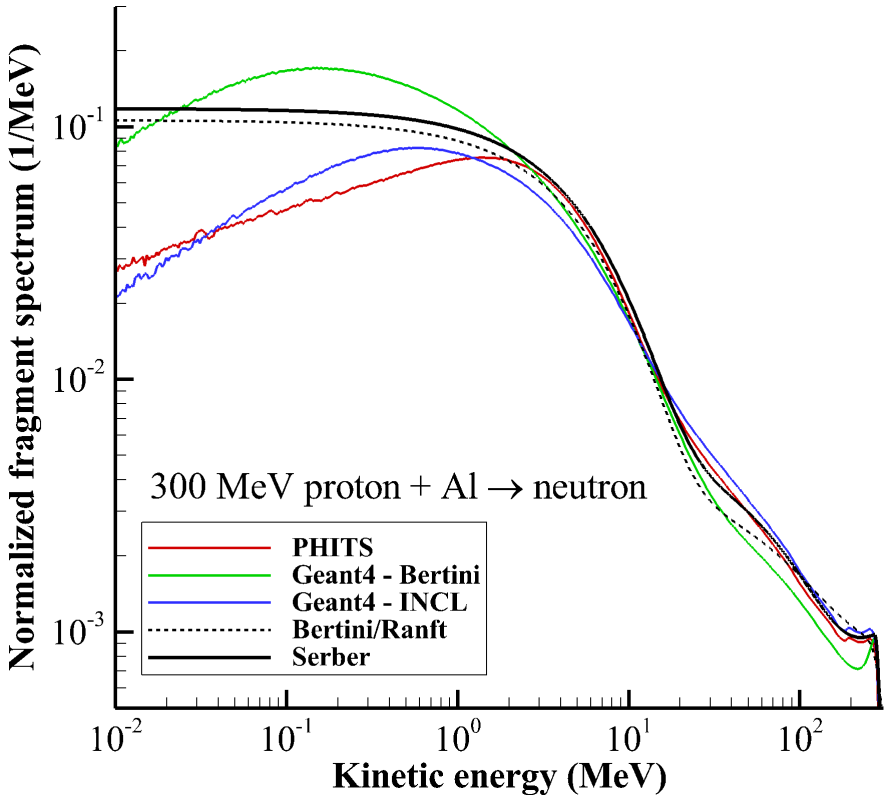

Figure 12: Comparison of spectral distributions for neutron production of 300 MeV protons projectiles on aluminum using the new Serber model, Bertini/Ranft original values (Wilson et al., 1988b), and the PHITS, Geant4-Bertini, and Geant4-INCL Monte Carlo results. Each of the model outputs was normalized to unity so that the differences in spectral shape could be studied.

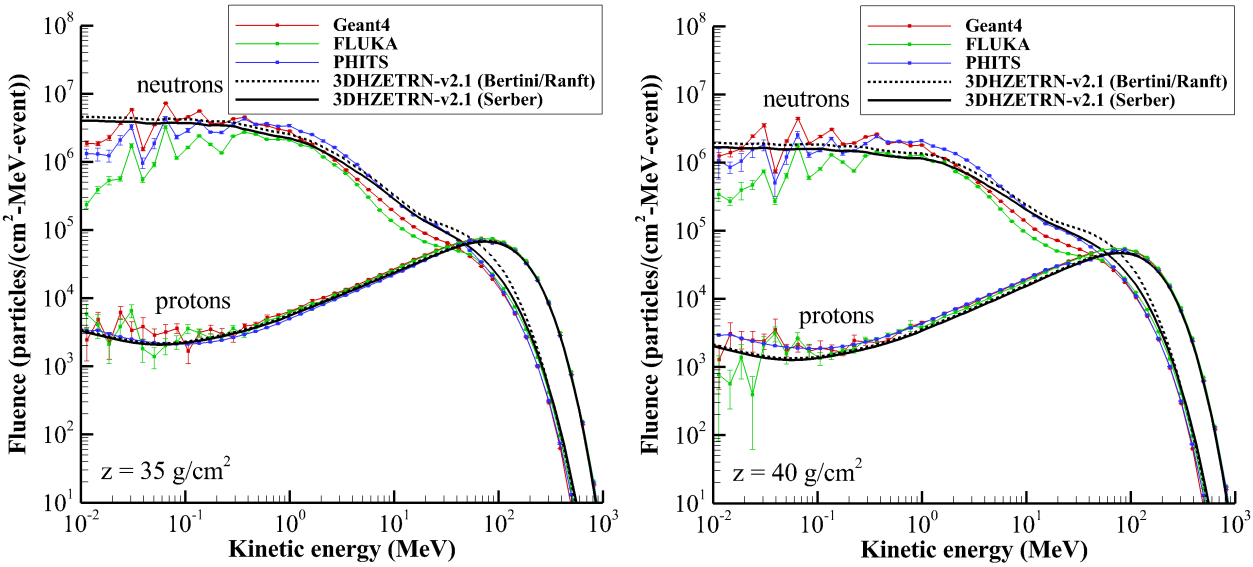

Figure 13: Impact of current Serber model contribution to neutron and proton fluence spectra in an aluminum sphere.

4.1. Monte Carlo Benchmarks

We now turn to benchmarking 3DHZETRN-v2.1, in which the added complications of 3D light-ion treatments have been addressed. Code verification uses an established benchmark consisting of a standard environment such as the Webber (1966) $P_0 = 100$ MV Solar Proton Event (SPE) spectrum with 10^9 protons/cm^2 with energies greater than 30 MeV as given in equation (54),

$$\phi_p(E) = \frac{10^9(E+938)}{200p(E)} e^{\frac{239.1-p(E)}{100}}, \tag{54}$$

in units of protons/cm^2 with $p(E) = \sqrt{E(E+1876)}$.

4.2. Webber SPE on an Aluminum Sphere

Upon implementation of equations (51) to (53), we again test with a benchmark. The shielding object is taken as a 40 g/cm^2 diameter aluminum sphere with the boundary condition being the Webber (1966) spectrum for the 23 Feb 1956 Solar particle event (not an accurate representation but a historically useful test spectrum with a 50 year history of usage) incident on the top of the sphere. The fluence on the center-line at 35 and 40 g/cm^2 depths are tabulated and presented in Fig. 13 with results from 3DHZETRN-v2.1 (Bertini/Ranft) (Wilson et al., 2017a) and results from three MC codes: Geant4 (Agostinelli et al., 2003), FLUKA (Fasso et al., 2005; Battistoni et al., 2007), and PHITS (Sato et al., 2006, 2013). While the proton spectrum at each of the evaluation points is little changed from prior results, the neutron spectra produced by 3DHZETRN-v2.1 (Serber) has moved into closer alignment with Geant4 results, especially in the 30 to 200 MeV region. It is clear from these results that the quasi-elastic contribution is better represented by use of the nuclear transport theory that includes Pauli exclusion effects.

4.3. Benchmark in an Inhomogeneous Cube and Sphere

The induced neutron and proton fluence spectra were evaluated in the aluminum/tissue combinations as 20/30/20 g/cm^2 in cubical (Fig. 14) and spherical (Fig. 15) geometry by three MC codes (Geant4,

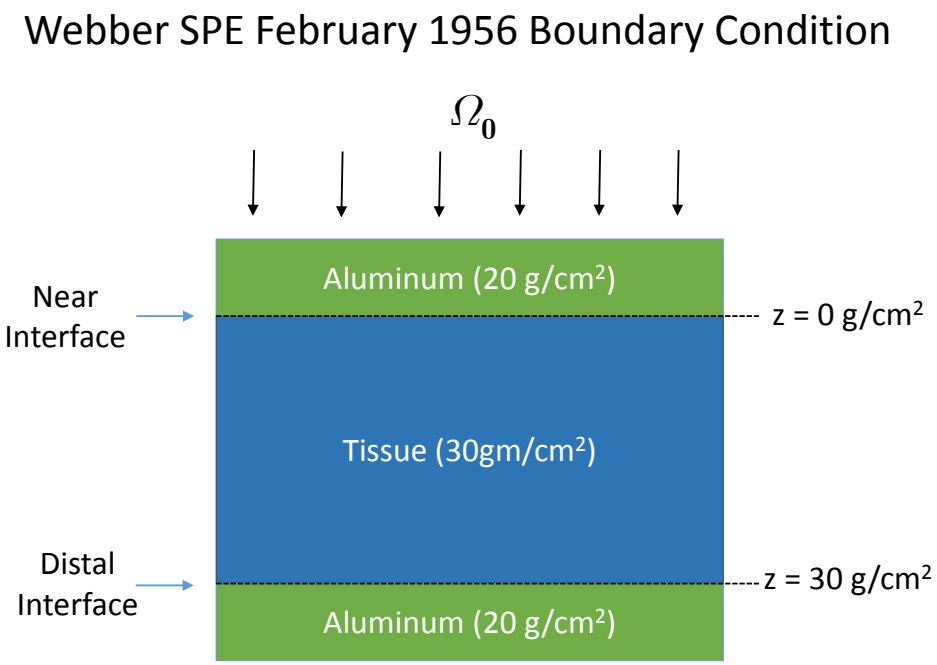

Figure 14: Aluminum shielded tissue cube exposed to Webber 1956 Solar Particle Event, Ω_0. The depth in tissue is represented by z, where $z = 0$ g/cm^2 is the near interface located at the top of the tissue slab, and $z = 30$ g/cm^2 is the distal interface located at the bottom of the tissue slab.

PHITS and FLUKA), 3DHZETRN-v2.1 (Bertini/Ranft), and 3DHZETRN-v2.1 (Serber), with the results at 0 and 30 g/cm^2 depths in the tissue shown in Fig. 16 for the finite slab geometry (cube) and Fig. 17 for the shielded spherical geometry. The proton fluence among the four codes is in reasonable agreement considering the different nuclear cross section sources. The larger discrepancy lies with the neutron spectra, especially at the bottom of the tissue cube ($z = 30$ g/cm^2) that is affected both by the penetration of the aluminum shield and overlying tissue. The results of the codes in a shielded tissue sphere in Fig. 17 are similar to that in the shielded tissue cube. The more dependable nuclear transport model of 3DHZETRN-v2.1 (Serber) is in better agreement with the MC codes, where improvements are significant at the bottom of the tissue ($z = 30$ g/cm^2).

The proton fluence predictions of the codes are in reasonable agreement above 1 MeV, but there are very large MC statistical uncertainties below 1 MeV (large error bars are not shown for protons below 1 MeV). The larger discrepancy lies with the neutron spectra, where disagreement among the MC results is on the same order as for 3DHZETRN-v2.1 (Serber). To further quantify differences among the codes, the neutron spectra is converted into effective dose using conversion factors for isotropic neutrons evaluated by Pelliccioni (2000) with FLUKA. The effective dose on the top and bottom of the tissue cube is given for neutrons in Table 2, and dose equivalent for protons is given in Table 3. The 3DHZETRN-v2.1 (Serber) model (N=30) compares reasonably well (about ten to fifteen percent) with the three MC codes. The 3DHZETRN-v2.1 (Serber) code (N=1) corresponds to the older HZETRN code and provides a conservative over-estimate, as expected. An additional measure of agreement is to evaluate the root mean square (RMS) relative differences in the neutron fluence from the four codes, as given in Table 4

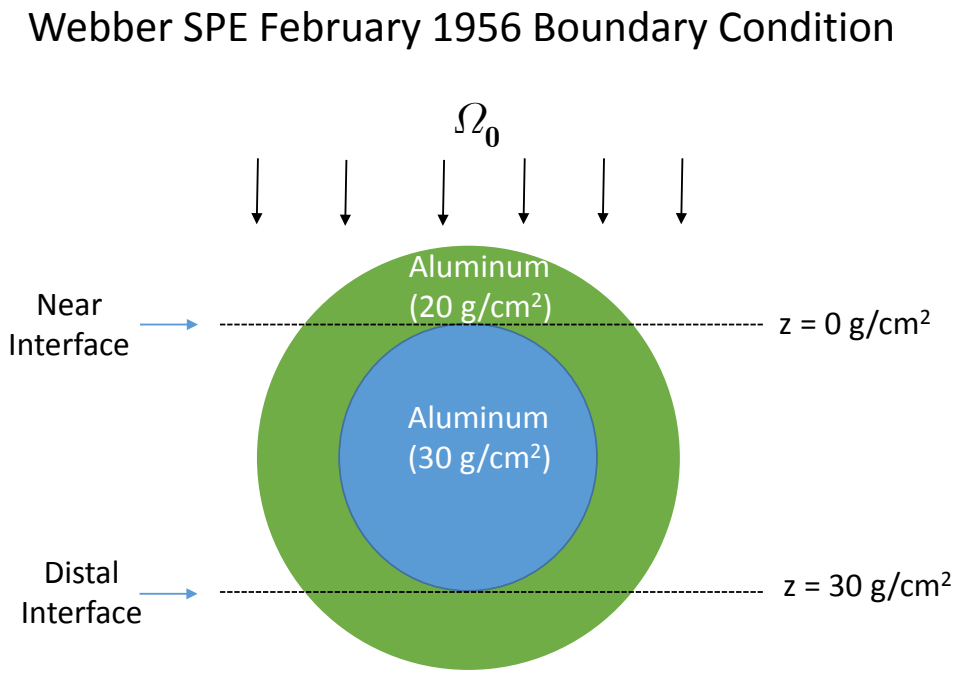

Figure 15: Aluminum shielded tissue sphere exposed to Webber 1956 Solar Particle Event, Ω_0. The depth in tissue is represented by z, where $z = 0$ g/cm^2 is the near interface located at the top of the tissue sphere, and $z = 30$ g/cm^2 is the distal interface located at the bottom of the tissue sphere.

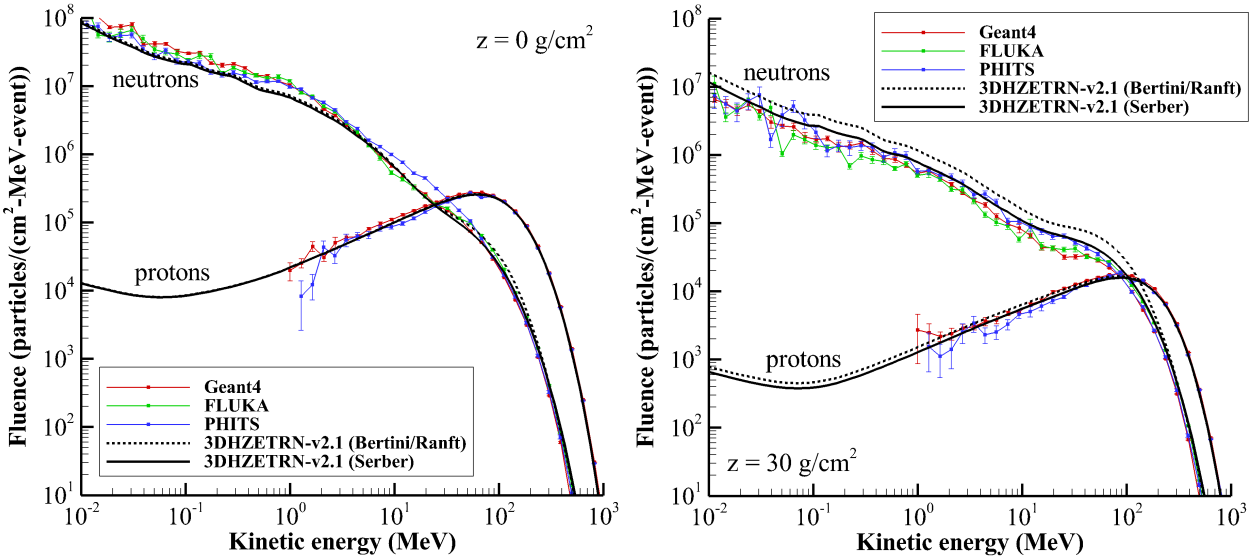

Figure 16: Webber SPE benchmark in cube geometry with N=30 compared with GEANT4, FLUKA, and PHITS at the near and distal interfaces.

Table 2: Neutron effective dose rates in cube geometry at top (z = 0 g/cm^2) and bottom (z = 30 g/cm^2) of ICRU tissue layer (mSv/event). Propagated MC statistical errors in neutron effective dose values were all less than 2%. 3DHZETRN refers to the 3DHZETRN-v2.1 (Serber) model developed in the present work.

z (g/cm^2)	3DHZETRN (N=1)	3DHZETRN (N=30)	Geant4	FLUKA	PHITS
0	13.37	9.38	10.30	10.78	13.0
30	4.78	2.51	1.73	1.88	2.19

on the top and the bottom of the tissue cube. A similar result is found for the RMS relative differences for the proton spectra among the four codes in Table 5. Again, it is observed that the agreement of 3DHZETRN-v2.1 with the MC codes is better than the agreement of the MC codes among themselves.

A principle difference in the three codes is the computational efficiency. The time required by the three codes to run these benchmarks is given in CPU seconds and is listed in Table 6. The 69 CPU seconds of 3DHZETRN-v2.1 (Serber) allows for the development of affordable means of design optimization software on a commercial laptop while Geant4, PHITS and FLUKA software requires a multiprocessing mainframe of more than a thousand processors to do a single evaluation within reasonable time (few days even for this very simple geometry). Still, Monte Carlo methods provide an important test point for developing codes capable of meeting operational and design requirements. Furthermore, computational speed has proven to be important for spaceflight validation in LEO where the time structure of the environment can be used to test various environmental components as was done using ISS and the Liulin instrument and other dosimetric instruments (Wilson et al., 2002, 2004, 2007). The main limitation on such studies is the uncertainty in the environmental models (especially for the trapped environment) as well as remaining uncertainty in nuclear cross sections (HZE induced reactions) and vehicle mass and material distributions.

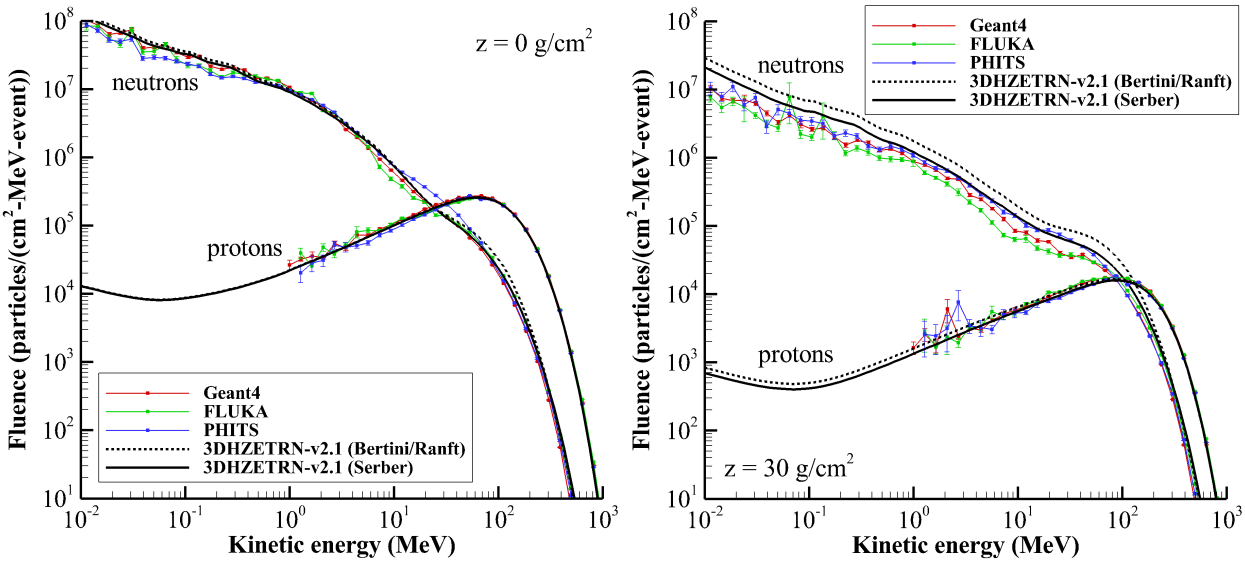

Figure 17: Webber SPE benchmark in spherical geometry with N=30 compared with GEANT4, FLUKA, and PHITS at the near and distal interfaces.

Table 3: Proton dose equivalent rates in cube geometry at top (z = 0 g/cm^2) and bottom (z = 30 g/cm^2) of ICRU tissue layer (mSv/event). Propagated MC statistical errors in proton dose equivalent values were all less than 10%. 3DHZETRN refers to the 3DHZETRN-v2.1 (Serber) model developed in the present work.

z (g/cm^2)	3DHZETRN (N=1)	3DHZETRN (N=30)	Geant4	FLUKA	PHITS
0	8.75	8.56	10.15	N/A	8.36
30	0.84	0.56	0.65	N/A	0.51

Table 4: Neutron fluence root mean square relative differences (dimensionless) of 3DHZETRN-v2.1 (Serber)and the MC codes at top (z = 0 g/cm^2) and bottom (z = 30 g/cm^2) of ICRU tissue layer in cube geometry.

z (g/cm^2)	vs Geant4	vs FLUKA	vs PHITS	MC spread
0	0.520	0.446	0.445	0.646
30	0.441	0.418	0.370	0.705

Table 5: Proton fluence (E > 1 MeV) root mean square relative differences (dimensionless) of 3DHZETRN-v2.1 (Serber) and MC codes at top (z = 0 g/cm^2) and bottom (z = 30 g/cm^2) of ICRU tissue layer in cube geometry.

z (g/cm^2)	vs Geant4	vs FLUKA	vs PHITS	MC spread
0	0.133	N/A	0.212	0.322
30	0.250	N/A	0.217	0.314

Table 6: Computer power requirements for current results (CPU seconds).

Code/Test case	3DHZETRN-v2.1	Geant4	PHITS	FLUKA
Webber SPE	69	2×10^8	1×10^8	1.8×10^8

5. Conclusions

The further development of improved transport procedures required advances in the nuclear model for nucleon-induced reactions in nuclei. An analytical treatment of the Serber model is shown to improve 3DHZETRN-v2.1 in the sense that the variance of the 3DHZETRN-v2.1 output for the Webber proton event model when compared to the results of three MC codes (Geant4, PHITS, and FLUKA) is significantly reduced, thereby facilitating focus on numerical algorithms for nucleon transport. This recent development of the Serber model may now be employed in future efforts that aim to improve the HZE interaction database that is generated by the NUCFRG code. Spectral improvements in a HZE Serber first step will be added in future transport developments.

6. Appendix: Solution to the Nuclear Transport Equation

The analytic solution of the transport equation used in the text depended on several assumptions:

a. $\sigma_m \equiv \sigma_m(E_0) \approx \sigma_m(E)$ for $E < E_0$
b. $\sigma \equiv \sigma(E_0) \approx \sigma(E)$ for $E < E_0$
c. $B \equiv B(E_0) \approx B(E)$ for $E < E_0$
d. $N(E_0) \equiv 1 - e^{-BE_0} \approx 1 - e^{-B(E)E} \equiv N(E)$ for $E < E_0$

In this Appendix, the effects of these assumptions will be examined.

The transport is described by a Volterra equation given as

$$\phi(z, E, E_0) = e^{-\rho\sigma_m(E)z} + \int_0^z e^{-\rho\sigma_m(E)(z-z')} \int_E^\infty \rho\sigma_m(E, E')\phi(z', E', E_0)dE'dz', \tag{55}$$

where the leading term is related to the boundary condition and describes the transport of the uncollided primary particles. The first estimate of the fluence is

$$\phi_0(z, E, E_0) = e^{-\rho\sigma_m(E)z}\delta(E - E_0). \tag{56}$$

Higher order corrections can be found by iterating the successive terms resulting from the Neumann series

solution of equation (55) as

$$\phi_n(z,E,E_0) = \int_0^z e^{-\rho\sigma_m(E)(z-z')} \int_{\epsilon_F}^{E_0-(\epsilon_F-\epsilon_a)} \rho\sigma(E') f_m(E,E') \phi_{n-1}(z',E',E_0) dE' dz', \tag{57}$$

where the spatial integral z' extends over 0 to z and the energy integral E' extends over E to $E_0-(\epsilon_F-\epsilon)$; the subscript m denotes Pauli blocking effects (in this Appendix we assume that the constituent nucleons are replaced by nucleons of the average energy ϵ_a). The first correction to the uncollided primary beam term of equation (56) is found by substituting $\phi_0(z,E,E_0)$ into the integral term on the right side of equation (57), resulting in

$$\begin{aligned}\phi_1(z,E,E_0) &= \int_0^z e^{-\rho\sigma_m(E)(z-z')} \int_{\epsilon_F}^{E_0-(\epsilon_F-\epsilon_a)} \rho\sigma_m(E,E') \phi_0(z',E',E_0) dE' dz' \\ &= z e^{-\rho\sigma_m(E_0)z} \rho\sigma(E_0) f_m(E,E_0).\end{aligned} \tag{58}$$

The first scattered nucleons from equation (58) are then given by the $\sigma_e(E,E')$ term as

$$\phi_{s1}(z,E,E_0) = z e^{-\rho\sigma_m(E_0)z} \rho\sigma(E_0) B(E_0) \left[\frac{e^{-B(E_0)(E_0-E)}}{1-e^{-B(E_0)E_0}}\right], \tag{59}$$

for E on the interval $\{\epsilon_F, E_0-(\epsilon_f-\epsilon_a)\}$, while the recoiling nuclear constituent produced by the first scattering is given by the $\sigma_r(E,E')$ term of equation (58) as

$$\phi_{r1}(z,E,E_0) = z e^{-\rho\sigma_m(E_0)z} \rho\sigma(E_0) B(E_0) \frac{e^{-B(E_0)E}}{1-e^{-B(E_0)E_0}}. \tag{60}$$

Note, these results in equations (59) and (60) were found under assumptions (a)–(d). Furthermore,

$$\int_{\epsilon_F}^{E_0-(\epsilon_F-\epsilon_a)} \phi_{s1}(z,E,E_0) dE = z e^{-\rho\sigma_m(E_0)z} \rho\sigma(E_0) F_P(E_0), \tag{61}$$

which is a functional form required for particle conservation. Clearly there are higher order terms for both the subsequent scattering of the incident nucleon as it moves through the target nuclear material with added recoiling nuclear constituents being produced. We now consider effects of various levels of approximations on the development of these additional multiple interaction terms resulting from the first interaction, as we have done before (Wilson et al., 1986, 2017b).

6.1. Multiple Scattering Series

To understand the scattering properties of the media, we only evaluate the $\sigma_e(E,E')$ terms in equations (58) and (59). We now follow the interactions of the multiple scattering that generally have further interactions prior to exit through the nuclear boundary. The next scattering term of the multiple scat-

tering series represents the second scattered term as

$$\phi_{s2}(z,E,E_0) = \int_0^z e^{-\rho\sigma_m(E)(z-z')} \int_{\epsilon_F}^{E_0-(\epsilon_F-\epsilon_a)} \rho\sigma(E') f_{me}(E,E') \phi_{s1}(z',E',E_0) dE' dz'$$

$$= \int_{\epsilon_F}^{E_0-(\epsilon_F-\epsilon_a)} \frac{\rho\sigma(E') f_{me}(E,E') \rho\sigma(E_0) f_{me}(E',E_0)}{\rho\sigma_m(E_0) - \rho\sigma_m(E)}$$

$$\times \left[\left(\frac{1 - e^{-\rho\sigma_m(E')z - \rho\sigma_m(E)z}}{\rho\sigma_m(E') - \rho\sigma_m(E)} \right) - \left(\frac{1 - e^{\rho\sigma_m(E_0)z - \rho\sigma_m(E')z}}{\rho\sigma_m(E_0) - \rho\sigma_m(E)} \right) \right] dE'. \tag{62}$$

Equation (62) can be evaluated numerically as a test on possible assumptions. Assumption (a), $\sigma_m \equiv \sigma_m(E_0) \approx \sigma(E)$, leads to

$$\phi_{s2}(z,E,E_0) = \int_0^z e^{-\rho\sigma_m(z-z')} \int_E^{E_0-(\epsilon_F-\epsilon_a)} \rho\sigma(E') f_{me}(E,E') z' e^{-\rho\sigma_m z'} \rho\sigma(E_0) f_{me}(E',E_0) dE' dz'$$

$$= \frac{z^2}{2} e^{-\rho\sigma_m z} \int_E^{E_0-(\epsilon_F-\epsilon_a)} \rho\sigma(E') f_{me}(E,E') z' e^{-\rho\sigma_m z'} \rho\sigma(E_0) f_{me}(E',E_0) dE'. \tag{63}$$

Additionally, assumptions (b) $\sigma \equiv \sigma(E_0) \approx \sigma(E)$ and (c) $B \equiv B(E_0) \approx B(E)$ simplify equation (63) to

$$\phi_{s2}(z,E,E_0) = \frac{(\rho\sigma z)^2}{2} e^{-\rho\sigma_m z} \int_E^{E_0-(\epsilon_F-\epsilon_a)} \frac{B e^{-B(E'-E)} B e^{-B(E_0-E')}}{N(E') N(E_0)} dE', \tag{64}$$

while assumption (d) $N(E_0) \equiv 1 - e^{-BE_0} \approx 1 - e^{-B(E)E} \equiv N(E)$ allows for a complete analytic solution of equation (57) as

$$\phi_{sn}(z,E,E_0) = \int_0^z e^{-\rho\sigma_m z} \int_E^{E_0-(\epsilon_F-\epsilon_a)} \rho\sigma_0(E,E') \phi_{sn-1}(z',E',E_0) dE' dz'$$

$$= \frac{[\rho\sigma B z]^n}{n!(n-1)! \left[1 - e^{-BE_0}\right]^n} e^{-B(E_0-E)} \left[E_0 - (\epsilon_F - \epsilon_a) - E\right]^{n-1} e^{-\sigma_m z}. \tag{65}$$

To evaluate the assumptions used in deriving the analytic result, we will compare the analytic solution with a numerical evaluation of the multiple scattering terms of equation (57). It is expected that the assumptions are most inappropriate at low energy. The multiple scattering solution is compared with the numerical evaluations (no assumptions) in Fig. 16 for 100 MeV initial energy. The adequacy of assumptions (a)–(d) are borne out even at very large penetration depths (especially at the higher energies) in the results in Fig. 16. Note the $\phi_{s1}(z,E,E_0)$ term is always the analytic solution given by (60) and never evaluated by a numerical procedure. This is the problem solved by Wilson et al. (1986) and is helpful in verifying the numerical codes (in this case the numerical evaluation of the perturbation terms). Similar results can be obtained for the initial recoiling particles (i.e., recoils from the collisions of the multiply scattered primary particle) as well.

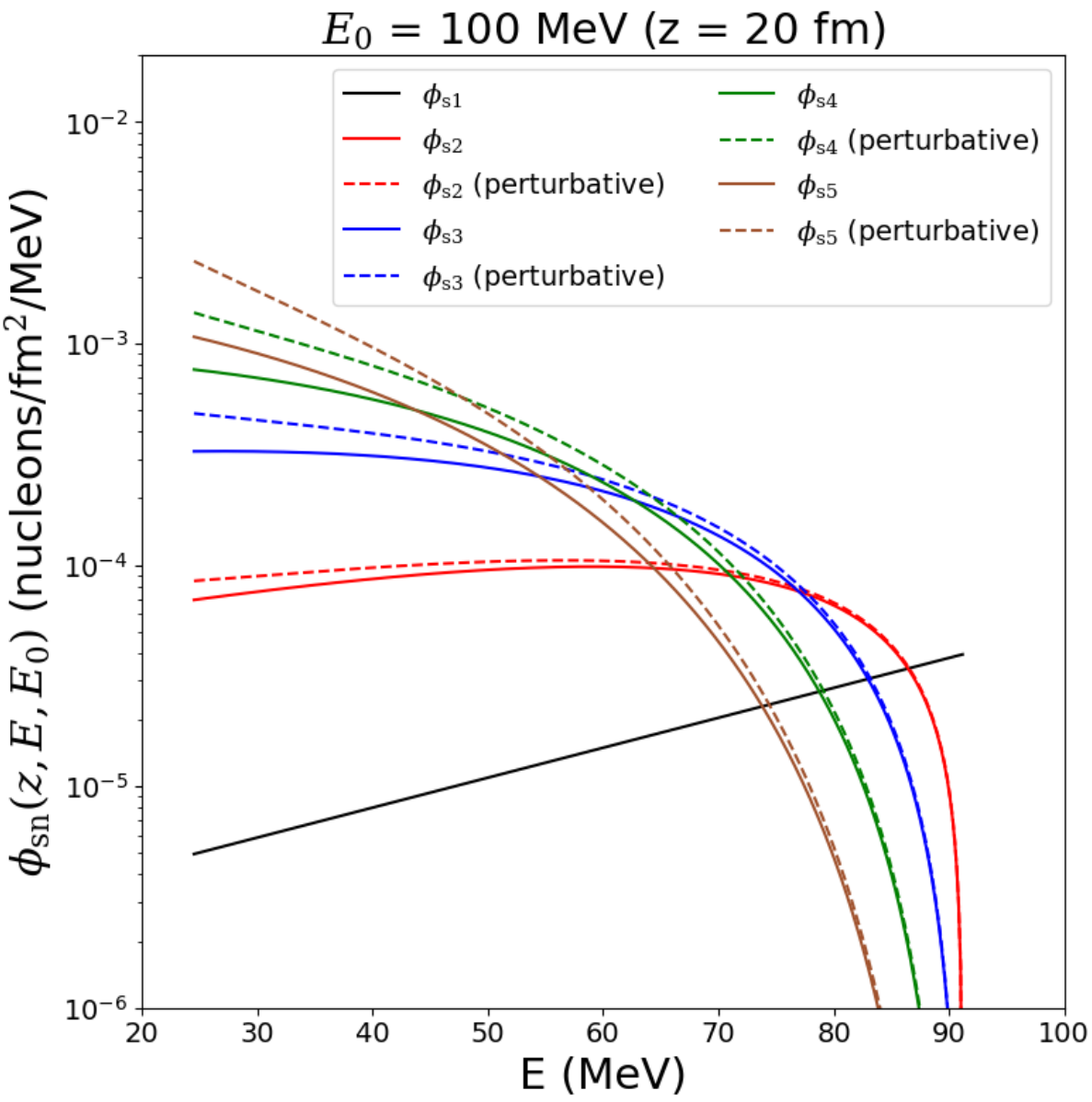

Figure 18: Numerical perturbation series and analytic approximation for nucleon transport in nuclear matter.

6.2. Multiple Recoil Series

We now consider the recoiling nucleons produced by collisions of the incident particle given by the $\sigma_r(E, E')$ term. Note, an additional subsequent recoil collision from the fluence of recoiling nucleons is inferior to the first recoil collision from the multiple scattering terms. The corresponding iterative terms are given by

$$\phi_{rn}(z, E, E_0) = \int_0^z e^{-\rho\sigma_m(E)(z-z')} \int_E^\infty f_{rm}(E, E')\phi_{sn-1}(z', E', E_0)dE'dz'. \tag{66}$$

Hence, the recoil source consists only of recoils produced by the transport of the incident nucleon in its multitude of collisions under assumptions (a)–(d) as

$$\phi_{rn} = \int_0^z e^{-\rho\sigma_m(z-z')} \int_E^\infty \rho\sigma_r(E, E')\phi_{sn}(z', E', E_0)dE'dz', \tag{67}$$

where the $\phi_{sn-1}(z, E, E_0)$ is the solution of the multiple scattering series in equation (65) above. The first production term results from the collisions of the uncollided incident particle, given as

$$\phi_{r1}(z, E, E_0) = \rho\sigma z e^{-\rho\sigma_m z} \left[\frac{e^{-BE}}{1 - e^{-BE_0}}\right], \tag{68}$$

and the higher order terms can be evaluated analytically. The result is

$$\phi_{rn}(z, E, E_0) = B\left[\rho\sigma z\right]^n e^{-\rho\sigma_m z} e^{-B[E+(\epsilon_F-\epsilon_a)]} \frac{\hat{a}_{n-2}\{B\left[E_0 - (\epsilon_F - \epsilon_a) - E\right]\}}{n!(n-2)!\left[1 - e^{-BE_0}\right]^n}, \tag{69}$$

where $\hat{a}_n(t)$ are special functions used in the nucleon-nucleus model by Wilson et al. (1986) with recurrence relations given by equations (37) and (38).

A graphical display for $\epsilon_a = 15.7$ MeV of the initial recoil series is given in Fig. 17 in comparison to the numerical implementation of the perturbation solution from equation (68). It is clear from the figure that the numerical implementation of the multiple recoil series is quite accurate and that use of the numerical perturbation series solutions are adequate for solving the more general equation (7) with energy independent interactions, as used in this Appendix. We now look to evaluation of the complete solution with energy independent interaction parameters using marching procedures and verify with the numerical perturbation series resulting in Fig. 17. In the text, we will implement a small correction for the $N(E)$ assumption and add a small correction for $N(E) \neq N(E_0)$.

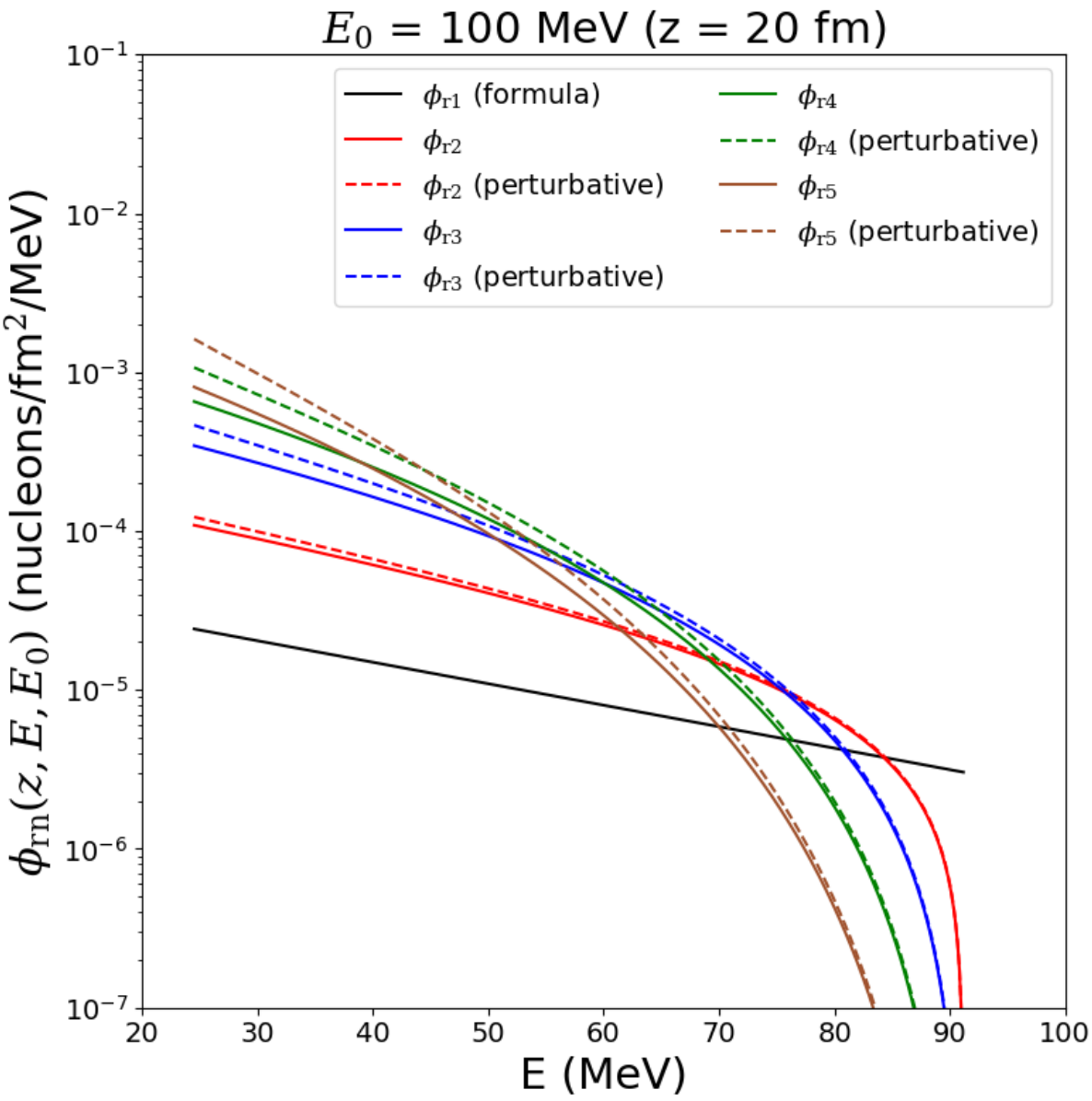

Figure 19: Numerical perturbation series and analytic approximation for nucleon recoils in nuclear matter.

References

Agostinelli, S., et al., 2003. Geant4–a simulation toolkit. *Nucl. Instrum. Methods Phys. Res. A* **506**, 250.

Alsmiller, R. G., 1967. High-energy nucleon transport and space vehicle shielding. *Nucl. Sci. Eng.* **27**, 158.

Anon., 1968. Intranuclear cascade code, 500-MeV protons on 0-16. I4C analysis codes (programmed for H. W. Bertini). Available from radiation shielding information center, Oak Ridge National Lab.

Battistoni, G., Muraro, S., Sala, P. R., Cerutti, F., Ferrari, A., Roesler, S., Fasso, A., Ranft, J., 2007. The FLUKA code: Description and benchmarking. *Proceedings of the Hadronic Shower Simulation Workshop 2006*, **896**, 31.

Bertini, H. W., 1969. Intranuclear-cascade calculation of the secondary nucleon spectra from nucleon-nucleus interactions in the energy range 340 to 2900 MeV and comparisons with experiment. *Phys. Rev.* **188**, 1711.

Bertini, H. W., Guthrie, M. P.; and Culkowski, A. H., 1972. Nonelastic interactions of nucleons and 1r-mesons with complex nuclei at energies below 3 GeV. ORNL-TM-3148, U.S. Atomic Energy Commission.

Chew, G. F., 1951. High energy elastic proton-deuteron scattering. *Phys. Rev.* **84**, 1057.

Clowdsley, M. S., Heinbockel, J., Kaneko, H., Wilson, J. W., Singleterry, R. C., Shinn, J. L., 2000. A comparison of the multigroup and collocation methods for solving the low-energy neutron Boltzmann equation. *Can. J. Phys.* **78**, 45.

Clowdsley, M. S., Shinn, J. W., Badavi, F. F., Heinbockel, J. H., Atwell, W., 2001. Neutron environment calculations for low Earth orbit. SAE 01ICES2327.

Dymarz, R., Kohmura, T., 1983. The mean free path of protons in nuclei and the nuclear radius. *Phys. Lett. B* **124**, 446.

Fasso, A., Ferrari, A., Ranft, J., Sala, P. R., 2005. FLUKA: A multiple-particle transport code. CERN-2005-10, INFN/TC 05/11, SLAC-R-773.

Geant4 Collaboration, 2012a. Geant4 reference physics lists.
Website: http://www.geant4.org/geant4/support/physicsLists/referencePL/referencePL.shtml.

Geant4 Collaboration, 2012b. Geant4 reference physics lists.
Website: http://www.geant4.org/geant4/support/physicsLists/referencePL/useCases.shtml.

Goldberger, M. L., 1948. The interaction of high energy neutrons and heavy nuclei. *Phys. Rev.* **74**, 1269.

Heinbockel, J. H., Feldman, G. A., Wilson, J. W., Singleterry, R. C., Leakeas, C. L., Clowdsley, M. S., 2003. Solutions to the low energy neutron Boltzmann equation for space. SAE 03ICES339.

Heinbockel, J. H., Slaba, T. C., Blattnig, S. R., Tripathi, R. K., Townsend, L. W., Handler, T., Gabriel, T. A., Pinsky, L. S., Reddell, B., Clowdsley, M. S., Singleterry, R. C., Norbury, J. W., 2009. Comparison of radiation transport codes, HZETRN, HETC and FLUKA, using the 1956 Webber SPE spectrum. NASA/TP-2009-215560.

Hofstadter, R., Collard, H. R., 1967. Nuclear Radii Determination by Electron Scattering. Landolt-Börnstein Series, Vol. 2, Springer-Verlag, Berlin-Heidelberg-New York.

Joos, G. 1958. *Theoretical Physics*, Hafner Publishing Co., New York.

Lamkin, S. L., 1974. A theory for high-energy nucleon transport in one-dimension. Master's thesis, Old Dominion University.

Matthiä, D., et al., 2016. The Martian surface radiation environment—a comparison of models and MSL/RAD measurements. *J. Space Weather Space Clim.* **6**, A13.

Metropolis, N., Bivins, R., Storm, M., Turkevich, A., Miller, J. M., Friedlander, G., 1958. Monte Carlo calculations on intranuclear cascades. I. Low-energy studies. *Phys. Rev.* **110**, 185.

Niita, K., Sato, T., Iwase, H., Nose, H., Nakashima, H., Sihver, L., 2006. PHITS—A particle and heavy ion transport code system. *Rad. Meas.* **41**, 1080.

Olive, K. A., et al., 2014. Particle Data Group, Review of Particle Data. *Chin. Phys.* **38**, 090001.

Pelliccioni, M., 2000. Overview of fluence-to-effective dose and fluence-to-ambient dose equivalent conversion coefficients for high energy radiation calculated using the FLUKA code. *Rad. Prot. Dosim.* **88**, 279.

Ranft, J., 1980. The FLUKA and KASPRO hadronic cascade codes. *Computer Techniques in Radiation Transport and Dosimetry*. Plenum Press.

Sato, T., Niita, K., Iwase, H., Nakashima, H., Yamaguchi, Y., Sihver, L., 2006. Applicability of particle and heavy ion transport code PHITS to the shielding design of spacecrafts. *Rad. Meas.* **41**, 1142.

Sato, T., Niita, K., Matsuda, N., Hashimoto, S., Iwamoto, Y., Noda, S., Ogawa, T., Iwase, H., Nakashima, H., Fukahori, T., Okumura, K., Kai, T., Chiba, S., Furuta, T., Sihver, L., 2013. Particle and heavy ion transport code system, PHITS, version 2.52. *J. Nucl. Sci. Technol.* **50**, 913.

Serber, R., 1947. Nuclear reactions at high energies. *Phys. Rev.* **72**, 1114.

Silberberg, R., Tsao, C. H., Shaprion, M. M., 1976. Semiemperical cross sections, and applications to nuclear interactions of cosmic rays. *Spallation Nuclear Reactions and their Applications*. B.S.P. Shen and M. Merker, eds, D. Reidel Publ. Co. 49.

Singleterry, R. C., Blattnig, S. R., Clowdsley, M. S., Qualls, G. D., Sandridge, C. A., Simonsen, L. C., Slaba, T. C., Walker, S. A., Badavi, F. F., Spangler, J. L., Aumann, A. R., Zapp, E. N., Rutledge, R. D., Lee, K. T., Norman, R. B., Norbury, J. W., 2011. OLTARIS: On-line tool for the assessment of radiation in space. *Acta Astronaut.* **68**, 1086.

Slaba, T. C., Blattnig, S. R., Badavi, F. F., 2010. Faster and more accurate transport procedures for HZETRN. *J. Comp. Phys.* **229**, 9397.

Slaba, T. C., Blattnig, S. R., Reddell, B., Bahadori, A., Norman, R. B., Badavi, F. F., 2013. Pion and electromagnetic contribution to dose: Comparisons of HZETRN to Monte Carlo results and ISS data. *Adv. Space Res.* **52**, 62.

Slaba, T. C., Wilson, J. W., Badavi, F. F., Reddell, B. D., Bahadori, A. A., 2016. Solar proton exposure of an ICRU sphere within a complex structure part II: Ray-trace geometry. *Life Sci. Space Res.* **9**, 77.

Slaba, T. C., Bahadori, A. A., Reddell, B. D., Singleterry, R. C., Clowdsley, M. S., Blattnig, S. R., 2017. Optimal shielding thickness for galactic cosmic ray environments. *Life Sci. Space Res.* **12**, 1.

Tripathi, R. K., Cucinotta, F. A., Wilson, J. W., 1997. Universal parameterization of absorption cross sections. NASA/TP-1997-3621.

Tripathi, R. K., Wilson, J. W., Cucinotta, F. A., 1998. Nuclear absorption cross sections using medium modified nucleon–nucleon amplitudes. *Nucl. Instrum. Methods Phys. Res. B* 145, 277.

Tripathi, R. K., Cucinotta, F. A., Wilson, J. W., 1999. Universal parameterization of absorption cross sections. NASA/TP-1999-209726.

Tripathi, R. K., Wilson, J. W., Cucinotta, F. A., 2002. A method for calculating proton-nucleus elastic cross-sections. *Nucl. Instrum. Methods Phys. Res. B* **194**, 229.

VerHage, J. E., Sandridge, C. A., Qualls, G. D., Rizzi, S. A., 2002. ISS radiation shielding and acoustic simulation using an immersive environment. *Immersive Projection Technology 2002 Symposium, Orlando, FL, March 24-25.*

Webber, W. R., 1966. An evaluation of solar-cosmic-ray events during solar minimum. D2-84274-1, Boeing Co.

Werneth, C. M., Xu, X., Norman, R. B., Ford, W. P., Maung, K. M., 2017. Validation of elastic cross section models for space radiation applications. *Nucl. Instrum. Methods Phys. Res. B* **392**, 74.

Wilson, J. W., 1973. Intermediate energy nucleon-deuteron elastic scattering. *Nucl. Phys. B* **66**, 221.

Wilson, J. W., Lamkin, S. L., 1974. Perturbation approximation to charged particle transport. *Trans. Am. Nucl. Soc.* **19**, 443.

Wilson, J. W., 1974. Multiple scattering of heavy ions, Glauber theory, and optical model. *Phys. Lett. B* **52**, 149.

Wilson, J. W., 1975. Composite particle reaction theory. Ph.D. thesis, College of William and Mary.

Wilson, J. W., Lamkin, S. L., 1975. Perturbation theory for charged-particle transport in one dimension. *Nucl. Sci. Eng.* **57**, 292.

Wilson, J. W., Costner, C., 1975. Nucleon and heavy ion total and absorption cross section for selected nuclei. NASA TN D-8107.

Wilson, J. W., 1977. Analysis of the theory of high-energy ion transport. NASA TN D-8381.

Wilson, J. W., Townsend, L. W., Bidasaria, H. B., Shimmerling, W., Wong, M., Howard, J., 1984. 20-Ne depth-dose relations in water. *Health Phys.* **46** 1101.

Wilson, J. W., Townsend, L. W., Cucinotta, F. A., 1986. Transport model of nucleon-nucleus reaction. NASA TM-87724.

Wilson, J. W., Townsend, L. W., Badavi, F. F., 1987a. A semi-empirical nuclear fragmentation model. *Nucl. Instrum. Methods Phys. Res. B* **18**, 225.

Wilson, J. W., Townsend, L. W., Badavi, F. F., 1987b. Galactic cosmic ray propagation in Earth's atmosphere. *Rad. Res.* **109**, 173.

Wilson, J. W., Townsend, L. W., Banapol, B., Chun, S. Y., Buck, W. W., 1988a. Charged-particle transport in one dimension. *Nucl. Sci. Eng.* **99**, 285.

Wilson, J. W., Chun, S. Y., Buck, W. W., Townsend, L. W., 1988b. High energy nucleon data bases. *Health Phys.* **55**, 817.

Wilson, J. W., Townsend, L. W., Schimmerling, W., Khandelwal, G. S., Khan, F., Nealy, J. E., Cucinotta, F. A., Simonsen, L. C., Shinn, J. L., Norbury, J. W., 1991. Transport methods and interactions for space radiations. NASA RP-1257.

Wilson, J. W., Townsend, L. W., Shinn, J. L., Cucinotta, F. A., Costen, R. C., Badavi, F. F., Lamkin, S. L., 1994. Galactic cosmic ray transport methods: Past, present, and future. *Adv. Space Res.* **14**, 841.

Wilson, J. W., Tripathi, R. K., Qualls, G. D., Cucinotta, F. A., Prael, R. E., Norbury, J. W., Heinbockel, J. H., Tweed, J., De Angelis, G., 2002. Advances in space radiation shielding codes. *J. Radiat. Res.* **43** (Suppl), S87–S91.

Wilson, J. W., Tripathi, R. K., Qualls, G. D., Tweed, J., 2004. Space radiation transport methods development. *Adv. Space Res.* **34**, 1319.

Wilson, J. W., Tripathi, R. K., Mertens, C. J., Blattnig, S. R., Clowdsley, M. S., 2005. Verification and validation: High Charge and Energy (HZE) transport codes and future development. NASA/TP-2005-213784.

Wilson, J. W., Tripathi, R. K., Badavi, F. F., Cucinotta, F. A., 2006. Standardized radiation shield design method: 2005 HZETRN. SAE/ICES paper 2006-01-2109.

Wilson, J. W., Nealy, J. E., Dachev, T. P., Tomov, B. T., Cucinotta, F. A., Badavi, F. F., De Angelis, G., Atwell, W., Leutke, N., 2007. Time serial analysis of the induced LEO environment within the ISS 6A. *Adv. Space Res.* **40**, 1562.

Wilson, J. W., Slaba, T. C., Badavi, F. F., Reddell, B. D., Bahadori, A. A., 2014a. 3D space radiation transport in a shielded ICRU tissue sphere. NASA/TP-2014-218530.

Wilson, J. W., Slaba, T. C., Badavi, F. F., Reddell, B. D., Bahadori, A. A., 2014b. A 3DHZETRN code in a spherical uniform sphere with Monte Carlo verification. NASA/TP-2014-218271.

Wilson, J. W., Slaba, T. C., Badavi, F. F., Reddell, B. D., Bahadori, A. A., 2014c. Advances in NASA radiation transport research: 3DHZETRN. *Life Sci. Space Res.* **2**, 6.

Wilson, J. W., Slaba, T. C., Badavi, F. F., Reddell, B. D., Bahadori, A. A., 2015. 3DHZETRN: Neutron leakage in finite objects. NASA/TP-2015-218692.

Wilson, J. W., Slaba, T. C., Badavi, F. F., Reddell, B. D., Bahadori, A. A., 2016. Solar proton exposure of an ICRU sphere within a complex structure part I: Combinatorial geometry. *Life Sci. Space Res.* **9**, 69.

Wilson, J. W., Slaba, T. C., Werneth, C. M., Badavi, F. F., Reddell, B. D., Bahadori, A. A., 2017a. Advances in NASA radiation transport: 3DHZETRN–v2. NASA/TP-2017-219665.

Wilson, J. W., Werneth, C. M., Slaba, T. C., Badavi, F. F., Reddell, B. D., Bahadori, A. A., 2017b. Neutron angular scatter effects in 3DHZETRN: Quasi-elastic. NASA/TP-2017-219597.

Wright, H. A., Anderson, V. F., Turner, J. E., Neufeld, J., Snyder, W. S., 1969. Calculation of radiation dose due to protons and neutrons with energies from 0.4 to 2.4 GeV. *Health Phys.* **16**, 13.

REPORT DOCUMENTATION PAGE

Form Approved
OMB No. 0704–0188

1. REPORT DATE *(DD-MM-YYYY)*	2. REPORT TYPE	3. DATES COVERED *(From - To)*
01-09-2019	Technical Publication	

4. TITLE AND SUBTITLE

Effects of the Serber First Step in 3DHZETRN-v2.1

5a. CONTRACT NUMBER

5b. GRANT NUMBER

5c. PROGRAM ELEMENT NUMBER

6. AUTHOR(S)

Wilson, John W.; Werneth, Charles M.; Slaba, Tony C.; Badavi, Francis F.; Reddell, Brandon; Bahadori, Amir A.; Sandridge, Christopher A.; Blattnig, Steve R.; Norman, Ryan B.

5d. PROJECT NUMBER

5e. TASK NUMBER

5f. WORK UNIT NUMBER

089407.01.23

7. PERFORMING ORGANIZATION NAME(S) AND ADDRESS(ES)

NASA Langley Research Center
Hampton, Virginia 23681-2199

8. PERFORMING ORGANIZATION REPORT NUMBER

L–21054

9. SPONSORING/MONITORING AGENCY NAME(S) AND ADDRESS(ES)

National Aeronautics and Space Administration
Washington, DC 20546-0001

10. SPONSOR/MONITOR'S ACRONYM(S)

NASA

11. SPONSOR/MONITOR'S REPORT NUMBER(S)

NASA–TP–2019–220401

12. DISTRIBUTION/AVAILABILITY STATEMENT

Unclassified-Unlimited
Subject Category 93
Availability: NASA STI Program (757) 864-9658

13. SUPPLEMENTARY NOTES

14. ABSTRACT

3DHZETRN-v2 includes a detailed three dimensional (3D) treatment of neutron/light-ion transport based on a quasi-elastic/multiple-production assumption allowing improved agreement of the neutron/light-ion fluence compared with results of three Monte Carlo (MC) codes in the sense that the variance with respect to the individual MC results is less than the variance among the MC code results. The current numerical methods are no longer the main limitation to HZETRN code development and further changes in the nuclear model are required. In a prior study, an improved quasi-elastic spectrum based on a solution of the transport approximation to nuclear media effects showed promise, but the remaining multiple-production spectrum was based on a database derived from the Ranft model that used Bertini multiplicities. In the present paper, we will implement a more complete Serber first step into the 3DHZETRN-v2 code, but we retain the Bertini-Ranft branching ratios and evaporation multiplicities. It is shown that the new Serber model in the 3HZETRN-v2 code reduces the variance with individual MC codes, which are largely due to nuclear cross section model differences.

15. SUBJECT TERMS

3D; HZETRN; Monte Carlo; Three dimensional

16. SECURITY CLASSIFICATION OF:			17. LIMITATION OF ABSTRACT	18. NUMBER OF PAGES	19a. NAME OF RESPONSIBLE PERSON
a. REPORT	b. ABSTRACT	c. THIS PAGE			STI Help Desk (email: help@sti.nasa.gov)
U	U	U	UU	51	19b. TELEPHONE NUMBER *(Include area code)* (757) 864-9658